

Clumpy vs. Extended Lyman Alpha Emitters at High Redshift

A dissertation submitted to the
Graduate College
of the University of Cincinnati
in partial fulfillment of the
requirements for the degree of

Doctor of Philosophy

in the Department of Physics
of the College of Arts and Sciences
by

Alexander Navarre

B.A. University of Illinois at Urbana-Champaign
May 2018

Committee Chair: Matthew Bayliss. Ph.D.

ABSTRACT

I present six strongly gravitationally lensed Ly α Emitters (LAEs) at $z \sim 4-5$ with HST narrowband imaging isolating Ly α . Through complex radiative transfer, Ly α encodes information about the spatial distribution and kinematics of the neutral hydrogen upon which it scatters. This information can help explain how star-forming galaxies contributed to Reionization. The primary goal of this work is to investigate the galaxy properties and Ly α morphologies of this sample. Many previous studies of high-redshift LAEs have been limited in Ly α spatial resolution. In this work I take advantage of high-resolution Ly α imaging boosted by lensing magnification, allowing for probing of sub-galactic scales that are otherwise inaccessible at these redshifts. I use broadband imaging from HST (rest-frame UV) and Spitzer (rest-frame optical) in SED fitting; providing estimates on the stellar masses ($\sim 10^8 - 10^9 M_\odot$), stellar population ages ($t_{50} < 40$ Myr), and amounts of dust ($A_V \sim 0.1 - 0.6$, statistically consistent with zero). I employ non-parametric star-formation histories to probe the young stellar-populations which create Ly α . I also examine the offsets between the Ly α and stellar continuum, finding small upper limits of offsets ($< 0''.1$) consistent with studies of low-redshift LAEs, indicating our galaxies are not interacting or merging. I find a bimodality in the sample's Ly α morphologies: clumpy and extended. Comparing these morphologies to the inferred galaxy properties, I find a suggestive trend: our LAEs with clumpy Ly α are generally younger than the LAEs with extended Ly α , suggesting a possible correlation with age. Finally, I present preliminary results from new, state of the art forward modeling code for one object in the sample. I find that intrinsic clump sizes between Ly α and the stellar continuum are statistically equivalent, possibly indicating the presence of ionized channels in the ISM.

ACKNOWLEDGMENTS

Support for HST program HST-GO-13639 was provided by NASA through a grant from the Space Telescope Science Institute, which is operated by the Association of Universities for Research in Astronomy, Inc., under NASA contract NAS 5-26555.

Based on observations made with the NASA/ESA Hubble Space Telescope, obtained at the Space Telescope Science Institute, which is operated by the Association of Universities for Research in Astronomy, Inc., under NASA contract NAS 5-26555. These observations are associated with programs HST-GO-9135, HST-GO-11974, HST-GO-13003, HST-GO-13639, HST-GO-14497.

This work is based in part on observations made with the Spitzer Space Telescope, which was operated by the Jet Propulsion Laboratory, California Institute of Technology under a contract with NASA. Support for the Spitzer programs used in this work was provided by NASA. Spitzer data used in this analysis were taken as a part of programs # 20754, # 60158, # 70154, and # 90232.

Some of the data presented in this paper were obtained from the Multimission Archive at the Space Telescope Science Institute (MAST): [10.17909/jvg9-v026](https://doi.org/10.17909/jvg9-v026).

DEDICATIONS

Over these past years of graduate study, I have done a lot. My work has challenged me in ways I could not have imagined when I started, yet nonetheless has been a joy to do. I have participated in every part of the academic life-cycle, from writing proposals to giving talks. The thing keeping me afloat through all of this has been the consistent and full support of my numerous mentors, teachers, friends, and family. Without them, I would not have been able to complete this work, and though doing so, grow as an individual.

I would like to first thank my wonderful advisor, Matthew Bayliss, who has gone above and beyond from day one. I am very grateful for all the time and effort spent in tutoring me, connecting me with others in the field, and providing me the opportunities to learn and share my work abroad. You were the steady hand through my first time writing a professional paper, and making a proposal for time on a space telescope; both nerve-wracking experiences. All the good work I have done is possible because of you.

Next, I want to thank all the members of the SGAS team, especially Gourav Khullar, Mike Gladders, Keren Sharon, Michael Florian, Jane Rigby, Josh Roberson, and Keunho Kim. From our discussions in the weekly group meetings to the jokes said at dinner at our meetups, you have fostered not only a space to learn and grow, but a community I am proud to be a part of.

I would also like to thank my professors at the University of Cincinnati, especially Rohana Wijewardhana, Richard Gass, and Colin Bischoff. Your tutelage has had a meaningful impact on my growth as an academic and as a person. You are scholars of the highest order, and I am continually in awe of your commitment to your students.

I would like to give special thanks to the staff of the physics department at the University of Cincinnati, especially Dara Miller, Diane Bolden, and Bethany Egbers. Your work behind the scenes deserves no understatement. I cannot imagine having to navigate the bureaucracy of being a graduate student without you.

Finally, I would like to say thank you to my family and friends. When I doubted myself you were always there to reassure me. When I needed an escape from work, you were always available. To say that I am lucky to have you in my life is an understatement. Thank you for everything.

Contents

1	Introduction	1
1.1	Initial Definitions	1
1.2	The Epoch of Reionization	3
1.3	Lya as a Tracer	5
1.3.1	Lya Radiative Transfer - Scattering	7
1.3.2	Lya Radiative Transfer - Doppler Shifts	9
1.4	Lya and LAEs	12
1.5	LAE Morphology	15
1.6	Gravitational Lensing	18
2	Data	21
2.1	Lensed LAE Sample	21
2.2	Sample Discovery and Spectroscopic Observations	24
2.3	HST Narrow-band Imaging	26
2.4	Broadband Imaging	27
2.4.1	HST	27
2.4.2	Spitzer	28
3	Methodology	29
3.1	Photometry	29
3.2	Stellar Population Synthesis Modelling with Prospector	33
3.3	Lens Models	39
3.4	Forward Modeling of Galaxy Morphology	40
3.5	Offset Measurements	44
3.6	Classification of Clumpy vs. Extended	45
4	Analysis	47
4.1	Inferred Galaxy Properties	47
4.2	Lya and UV Spatial Coincidence	49

4.3 LAE Morphology	49
4.4 Preliminary Forward Modeling of L1	51
5 Summary	53

List of Figures

1	Extinction vs. Attenuation	2
2	History of the Universe	4
3	Ly α Transmission vs. Redshift	6
4	$f_{esc,LyC}$, Ly α EW, and Ly α Peak Separation	7
5	Simulated Ly α Surface Brightness for a High-Redshift SFG	9
6	Methods of Ly α and LyC Escape	10
7	Ly α Spectra in the Expanding Shell Model	11
9	Ly α and LyC in a Realistic Star Forming Region	14
10	LARS galaxy LAE Morphologies	16
11	Gravitational Lensing Formalism	19
12	LAE Sample: Lensing Cluster and Postage Stamp Views	21
13	LAE Spectra Centered on Ly α	23
14	HST Encircled Energy	30
15	SED Modeling and Non-Parametric SFHs	36
16	Forward Modeling Code Flowchart	41
17	Emcee Posterior Distribution Example	42
18	Source Plane Model of L1	43
19	LAE Luminosities	46
20	LAE Ly α Imaging and Morphology	47
21	Forward Modeling Output for L1	52

List of Tables

1	Positions and Redshifts of Lensed LAEs and Lensing Clusters	22
2	Narrowband Ly α Ramp Filter Observations	24
3	Photometric AB Magnitudes	25
4	Overview of LAE UV and Ly α Properties	26
5	Inferred Galaxy Properties from Prospector	39
6	Angular Offsets Between Ly α and Stellar Continuum	45
7	Best-Fit Sérsic Parameters for L1	51

1. INTRODUCTION

1.1. *Initial Definitions*

As the universe expands, it stretches the wavelength of photons within it. This effect is only seen on cosmological timescales and is known as cosmological redshift. It is represented with the letter z , which will herein be referred to as redshift unless otherwise stated. We define redshift as the change in wavelength divided by the wavelength. Defining the emitted and observed wavelengths as the wavelength of the photon when it was emitted and observed, we get equation (1). Note that $1 + z$ is the measure used at the bottom of [Figure 2](#). For example, a photon with a redshift $z = 6$ has a seven times larger observed wavelength than when it was emitted.

$$z = \frac{\Delta\lambda}{\lambda} \rightarrow 1 + z = \frac{\lambda_{observed}}{\lambda_{emitted}} \quad (1)$$

In this work I refer to the interstellar medium (ISM), the circumgalactic medium (CGM) and the intergalactic medium (IGM). The interstellar medium is the region between star systems within a galaxy. It contains multi-phase gas and dust. The circumgalactic medium is a halo of diffuse gas that surrounds a galaxy. No stars are located in the CGM, but this material serves as a reservoir for star formation. The intergalactic medium is the space between galaxies, and is even less dense than the CGM.

Dust, as referenced above, is made up of solid molecules of sizes generally less than $100\mu\text{m}$. They are initially formed in the atmospheres of post-main-sequence stars and in supernovae. Through various physical processes, they evolve and grow in size either in star-forming systems or in the ISM ([Salim & Narayanan 2020](#)). For the context of this work, dust primarily acts as a source of extinction for UV and optical light. That is to say that dust grains scatter photons out of our line of sight, or absorb them and re-emit their energy in millimeter wavelengths. We calculate the amount of dust extinction through the parameter A_V : the amount of magnitudes less flux density that would be observed in the V-band due to dust. The V-band is a name for a historical photometric filter that selects wavelengths roughly between 500nm and 700nm.

The difference between extinction and attenuation should also be noted. Extinction, as described above, is the combined processes of scattering and absorption (and re-emission at redder wavelengths). Attenuation includes the properties of extinction, but also accounts for interactions with complex gas and dust geometries. Attenuation includes the effects of light scattering into the line of sight, varying densities of gas and dust, and contributions from obscured stars within gas clouds (Salim & Narayanan 2020). These processes are described in Figure 1.

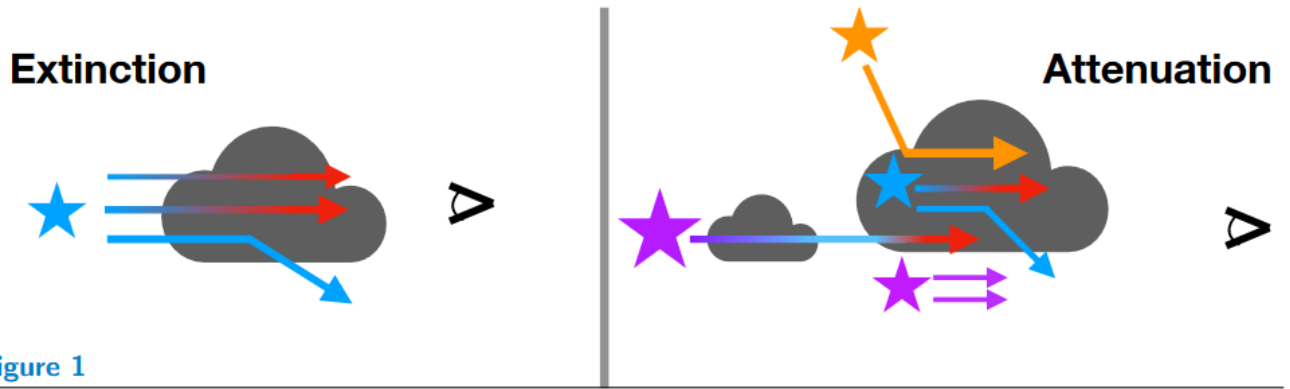


Figure 1

Figure 1: Figure 1 from Salim & Narayanan (2020) describing the differences between extinction and attenuation. The color of the arrows corresponds with their wavelengths, with blue being shorter (UV and/or optical) and red being longer (IR and/or millimeter). The shape on the right represents our detector.

Doppler shifts describe the change in the wavelength (or equivalently, frequency) seen by an observer who is moving with respect to the wave source. In the context of this work, the wave sources are photons and the Doppler Shifts come from photons interacting with neutral hydrogen. For example: A photon scattering off of a moving neutral hydrogen atom. Unlike objects in classical physics, photons always travel at the speed of light, regardless of reference frame. Obeying this law of special relativity results in the neutral hydrogen atom "seeing" the photon with a different wavelength than what would be observed in the lab. The Doppler Shift is calculated as:

$$\frac{\lambda_r}{\lambda_s} = \frac{f_s}{f_r} = \sqrt{\frac{1 + \beta}{1 - \beta}} \quad (2)$$

for velocities in the longitudinal direction and as:

$$f_r = \gamma f_s \quad (3)$$

or

$$f_r = \frac{f_s}{\gamma} \quad (4)$$

for velocities in the transverse direction. Equation (3) represents a blueshift (hydrogen moving towards photon), and equation (4) represents a redshift (hydrogen moving away from photon). The subscripts r and s refer to the source and receiver. In our example, the source is the photon and the receiver is the hydrogen atom. β and γ are relativistic quantities dependent on the relative velocity of the source and receiver v .

$$\beta = \frac{v}{c} \quad (5)$$

$$\gamma = \frac{1}{\sqrt{1 - \beta^2}} = \frac{1}{\sqrt{1 - \left(\frac{v}{c}\right)^2}} \quad (6)$$

Equivalent Width (herein EW) is a measure of the strength of an emission or absorption line. For a line flux density f_l and a continuum flux density f_c , the EW W_λ of the line is calculated as:

$$W_\lambda = \int \frac{|f_l(\lambda) - f_c(\lambda)|}{f_c(\lambda)} d\lambda \quad (7)$$

The absolute value is used so that both emission lines and absorption lines produce positive values.

1.2. The Epoch of Reionization

At the earliest times the universe was a dense plasma of elementary particles. As the universe expanded and cooled, these particles combined to form hydrogen and helium atoms in a process known as Recombination ($z \sim 1100$). During the following era ($(1100 < z < 20$, Dark Ages), before the first stars had formed, the matter content of the universe was composed of wholly neutral

gas. Here neutral means that the atoms (mostly Hydrogen) have captured electrons. Over time overdensities in the neutral gas condensed, setting the stage for formation of stars and galaxies. The Epoch of Reionization ($z \sim 20 - 6$, EoR) refers to the era where the first stars and galaxies formed. During this era, the universe underwent a phase transition where the intergalactic medium (IGM) went from wholly neutral to wholly ionized. How exactly the universe ionized the IGM in this era is an outstanding problem in modern astronomy.

There are two leading theories explaining the mechanism of this phase transition: Lyman-Continuum (LyC) photon escape from star-forming galaxies (SFGs) and Active Galactic Nuclei (AGN). LyC photons are photons that have wavelengths $\lambda < 912 \text{ \AA}$, corresponding to the energy required to ionize hydrogen: 13.6 eV. Both SFGs and AGNs produce large amounts of LyC radiation, but their relative contributions to reionization are unclear.

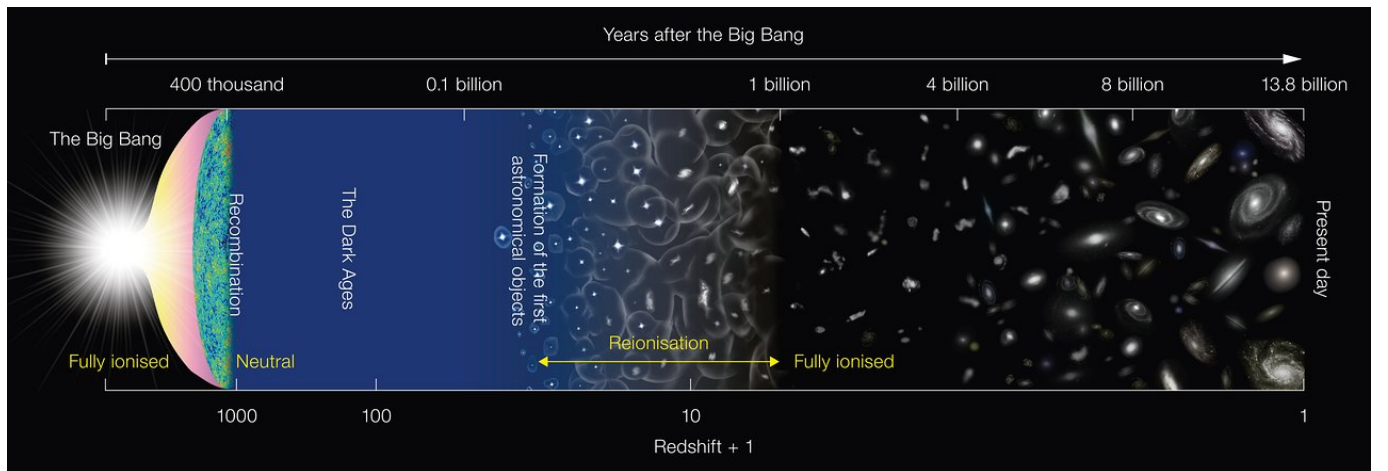


Figure 2: A cartoon picture of the history of the universe. The top axis shows time since the big bang, and the bottom axis shows $1+\text{redshift}$: a quantity used as a proxy for lookback time (looking backwards in time from today). This illustration emphasizes the reionization of the universe. This period was called the Epoch of Reionization and is when the IGM went from neutral to ionized. Ionization fronts around the first galaxies are shown and merge as time progresses. This image is a press release image created by the European Southern Observatory. It is licensed under the Creative Commons Attribution 4.0 International License, which allows for reproduction provided credit is clear and visible.

Some recent studies (Masters et al. 2012; Palanque-Delabrouille, N. et al. 2013; Ricci et al. 2016; Matsuoka et al. 2023) show that AGN number density falls drastically as redshift approaches $z = 6$. This suggests that they likely contribute less than 30% of the total ionizing photons required to reionize the IGM. However, Madau & Haardt (2015) constructed an AGN-dominated model scenario that is consistent with multiple observational constraints. Additionally, recent results from the RUBICON survey find that quasars could contribute $\sim 50 - 100\%$ of the ionizing photon budget at the end of the EoR (Grazian et al. 2023). The astronomical community currently does not have a consensus on the (non)dominance of AGNs during the EoR.

For the other candidate—SFGs—LyC emission is consistently observed in many galaxies in the local universe up to $z \sim 2$ (see Figure 3). Above this, direct detection of LyC becomes difficult, but tracer properties estimate LyC escape up to very high redshifts. However, f_{esc} —the fraction of LyC photons that escape from their host galaxy—is often calculated to be smaller than expected for SFG-dominated scenarios. This points to a need for further understanding of LyC production and escape from SFGs (Robertson 2022, and references therein). In the next subsection I discuss why one might find low LyC escape fractions from SFGs, and how Lyman-Alpha can help find LyC leaking galaxies.

1.3. *$\text{Ly}\alpha$ as a Tracer*

Direct detection of LyC is difficult at $z \sim 2 - 4$, and effectively impossible above $z \sim 4.5$ due to the IGM becoming opaque to LyC photons (Madau 1995; Inoue et al. 2014). Determining the properties of LyC escape at high redshifts thus requires use of indirect tracers such as Lyman-Alpha (herein $\text{Ly}\alpha$) Equivalent Width (EW), $\text{Ly}\alpha$ escape fraction, or $\text{Ly}\alpha$ peak separation. $\text{Ly}\alpha$ is emitted from the atomic transition $n = 2$ to $n = 1$ of hydrogen, and is hydrogen’s brightest recombination line. $\text{Ly}\alpha$ is created in abundance from the same stellar populations that create LyC photons (Dijkstra 2017), and abundantly appears in many young SFGs.

Studies find that $\text{Ly}\alpha$ diagnostics such as $\text{Ly}\alpha$ EW and peak separation are linked to LyC escape, at both low (Alexandroff et al. 2015; Izotov et al. 2018, 2021; Hu et al. 2023) and high redshifts (Steidel et al. 2018; Kramarenko et al. 2023; Roy et al. 2023). $\text{Ly}\alpha$ EW as a tracer is the easier of

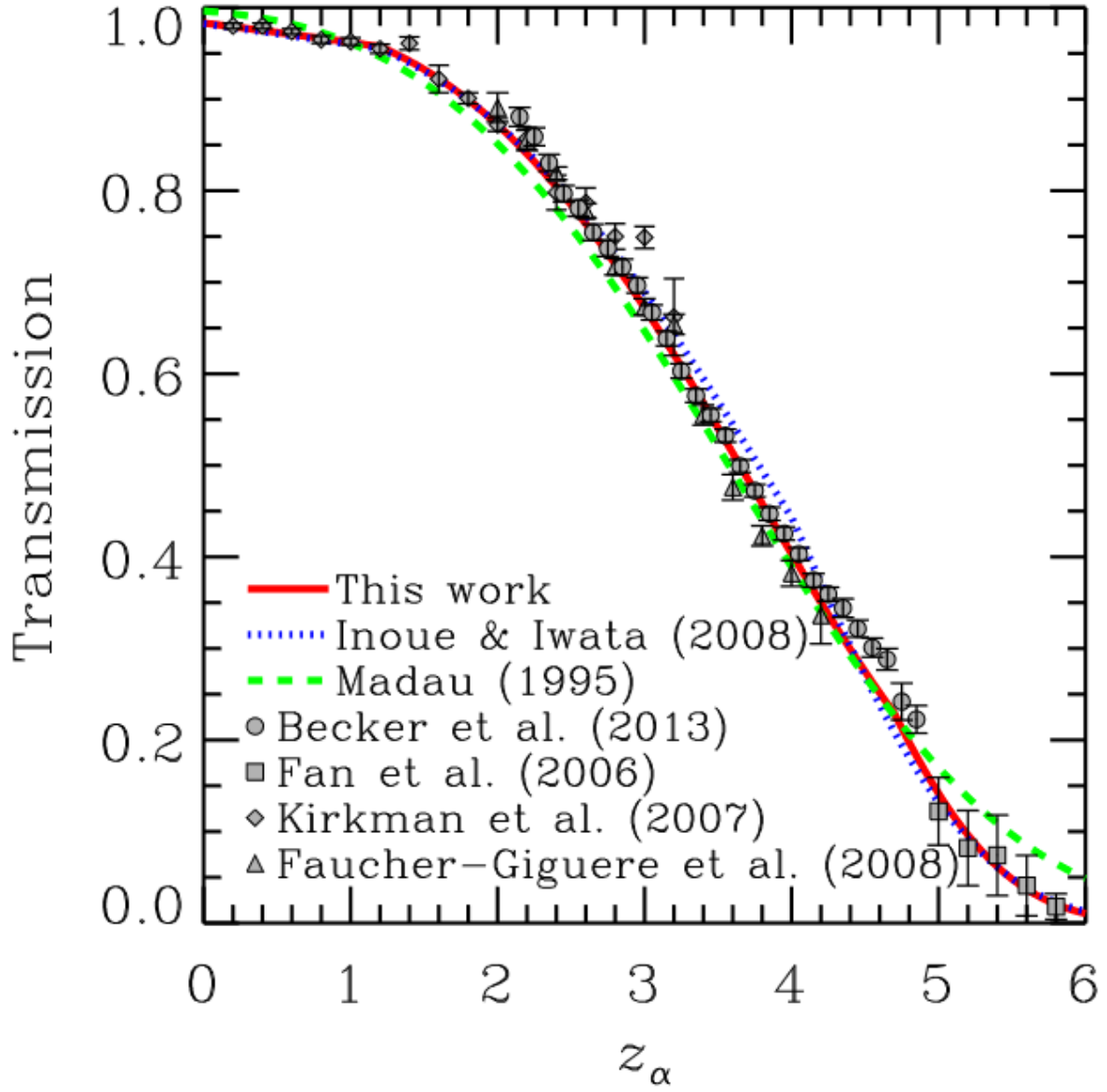


Figure 3: Figure 5 from Inoue et al. (2014). The y-axis describes the fraction of Ly α photons that would reach us given that they escaped their host galaxy at the redshift of the x-axis. Since LyC photons are attenuated by the same neutral hydrogen as Ly α this curve can also be applied to LyC transmission. One can see that as redshift increases, the transmission quickly drops.

the two to understand. Larger Ly α EW indicates a larger production of LyC photons, since both LyC and Ly α are created in the same environments by the same stars. Simply put, the more LyC photons that are created, the more probable it is that some will escape. However, understanding

why Ly α peak separation is a good tracer is more involved. Analysis of Ly α emission (especially on sub-galactic scales) is complicated due to a set of non-trivial radiative transfer processes (Dijkstra 2017). Ly α emission properties are highly dependent on the structure and kinematics of a galaxy's neutral gas (Heckman et al. 2011; Rivera-Thorsen et al. 2017; Chisholm et al. 2018; Gazagnes et al. 2018; Steidel et al. 2018; Kramarenko et al. 2023). Below I discuss Ly α radiative transfer and how its effects can be used to understand LyC escape.

1.3.1. Ly α Radiative Transfer - Scattering

The most important property of Ly α radiative transfer is that Ly α is isotropically scattered by neutral hydrogen. This is unlike LyC which undergoes extinction when interacting with neutral hydrogen. A hydrogen atom will absorb a Ly α photon, raising its electron energy level from the ground state $n = 1$ to the first excited state $n = 2$. But this state is unstable, and the electron quickly falls back to the ground state. When this happens, a new Ly α photon is emitted in a random direction. Although a new photon is created, it is effectively a scattering of the original photon.

The simplest conceptual path for a Ly α photon to take is direct escape from the galaxy after its initial creation. However, we see in many SFGs that the Ly α emission is spatially extended and/or

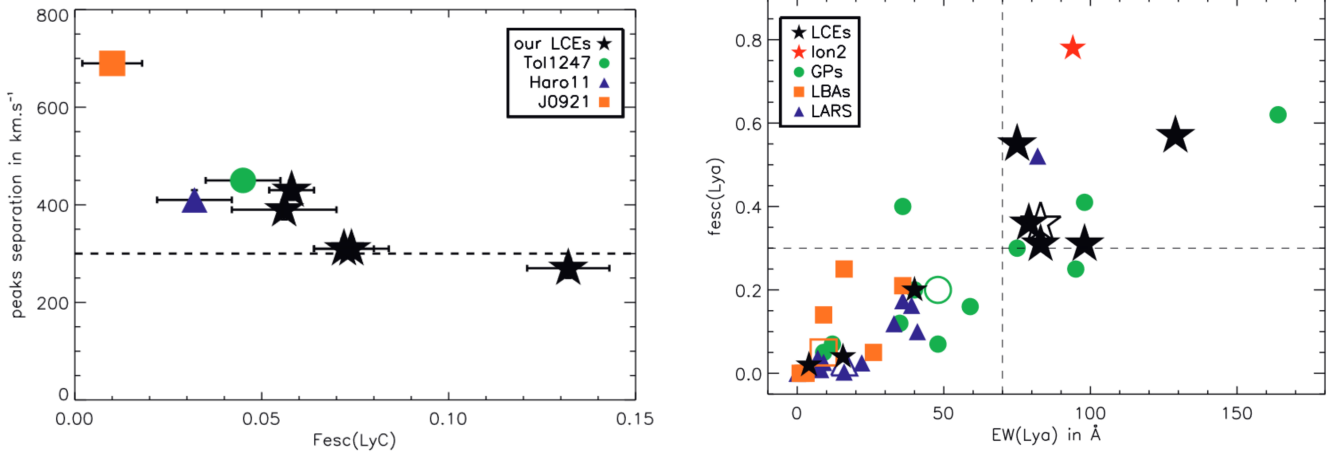


Figure 4: Figure 1 and part of Figure 5 from Verhamme et al. (2017). **Left:** Observations of a negative correlation between LyC escape fraction and Ly α peak separation. **Right:** Observations showing a positive correlation between Ly α equivalent width and LyC escape fraction.

offset from the associated stellar continuum (Östlin et al. 2009; Hayes et al. 2013; Runnholm et al. 2023). This happens because the Ly α photons interacted with neutral hydrogen atoms in-between their initial creation and escape. They scatter many times before they are able to escape the galaxy, allowing the Ly α photon to travel far from its original creation site. This leads to Ly α emission that is spatially broader than the stellar continuum. Figure 5 shows a simulated surface brightness map of Ly α for a high-redshift SFG. It was created with the radiative transfer code RASCAS (Michel-Dansac et al. 2020). The scale of the simulation includes the CGM, and shows an extended profile of Ly α across many brightness orders of magnitude.

A SFG with Ly α emission that is not extended and isotropic implies that there are few paths for Ly α to escape into the CGM along. It could also mean that there were significant amounts of dust, leading to strong Ly α extinction. In the first case, one explanation is that Ly α escapes along a small opening either due to low densities of neutral hydrogen, a gap in the neutral hydrogen distribution, or an ionized channel. These three methods for Ly α (and consequently LyC) escape are shown in Figure 6. Although, escape through realistic distributions of neutral hydrogen is likely a combination of all three types.

As described by Figure 6, models of LyC escape generally fall into two camps: ionization bounded escape (Zackrisson et al. 2013; Verhamme, Anne et al. 2015; Gronke et al. 2016; Rivera-Thorsen et al. 2017; Kim et al. 2023, Owens et al. (in prep)), and density bounded escape (Jaskot & Oey 2014; Gronke et al. 2015; Verhamme, Anne et al. 2015). Ionization bounded escape occurs when regions of LyC production are not fully surrounded by neutral hydrogen in the ISM; either through clumpy distributions or ionized channels. Density bounded escape occurs when the neutral hydrogen density is low enough to not completely attenuate LyC along a line of sight. Since Ly α has a much larger interaction cross-section with neutral hydrogen than LyC, direct escape of Ly α will preferentially occur along lines of sight that allow for LyC escape. Recent results from Kramarenko et al. (2023) suggest that a combination of both ionization-bounded and density-bounded models is required to robustly reproduce Ly α spectra.

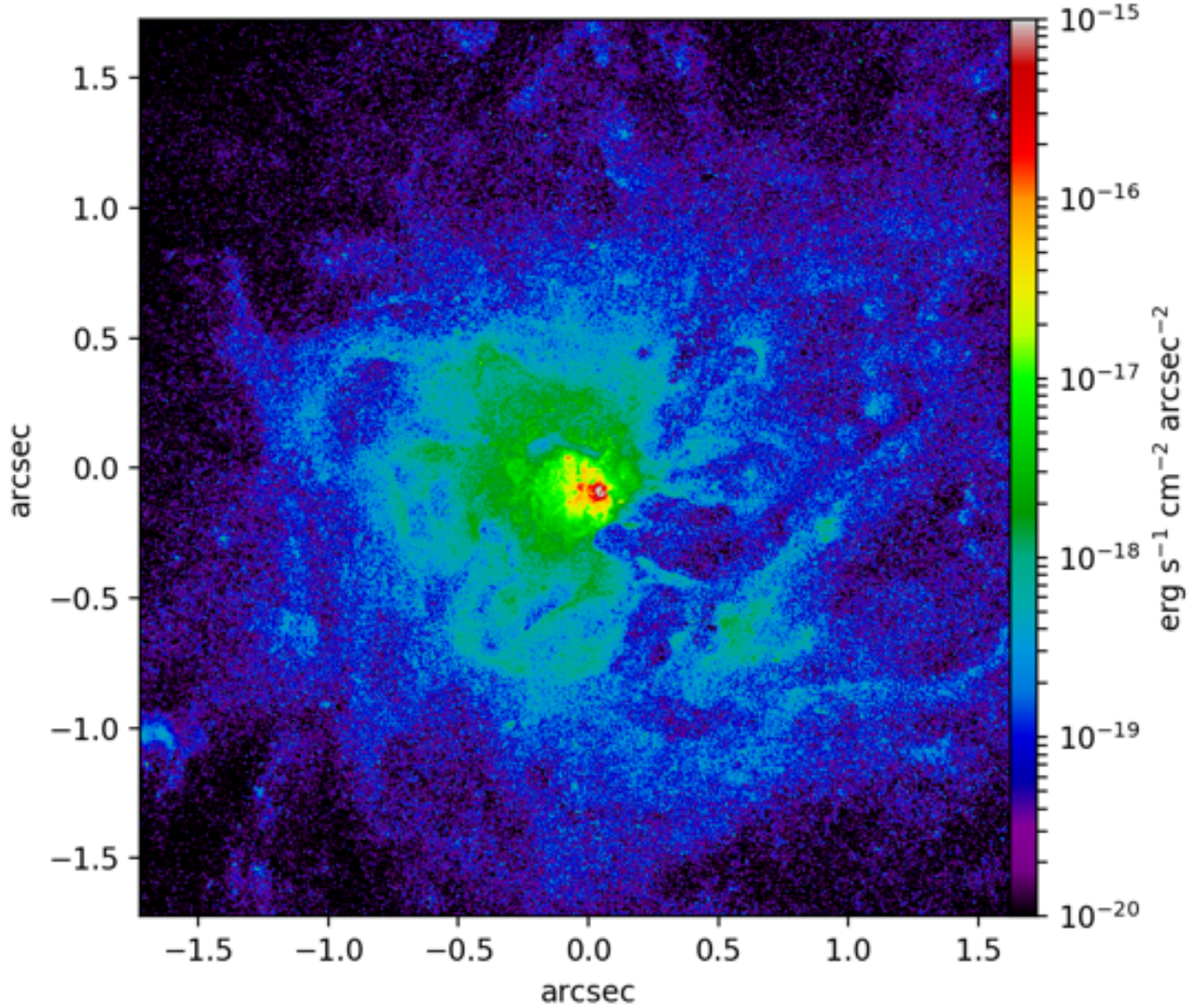


Figure 5: Figure 12 from Michel-Dansac et al. (2020). The simulated Ly α surface brightness for a high-redshift ($z \sim 4$) SFG. The simulation is centered on the galaxy and includes scales going out through the CGM. This shows increasingly faint extended Ly α emission beyond the core of the galaxy. Note the color bar is on a logarithmic scale.

1.3.2. Ly α Radiative Transfer - Doppler Shifts

The other major property of Ly α radiative transfer is Doppler Shifts. Doppler Shifts occur when scattering off of flowing gas and shift Ly α 's wavelength away from scattering resonance. Similar to

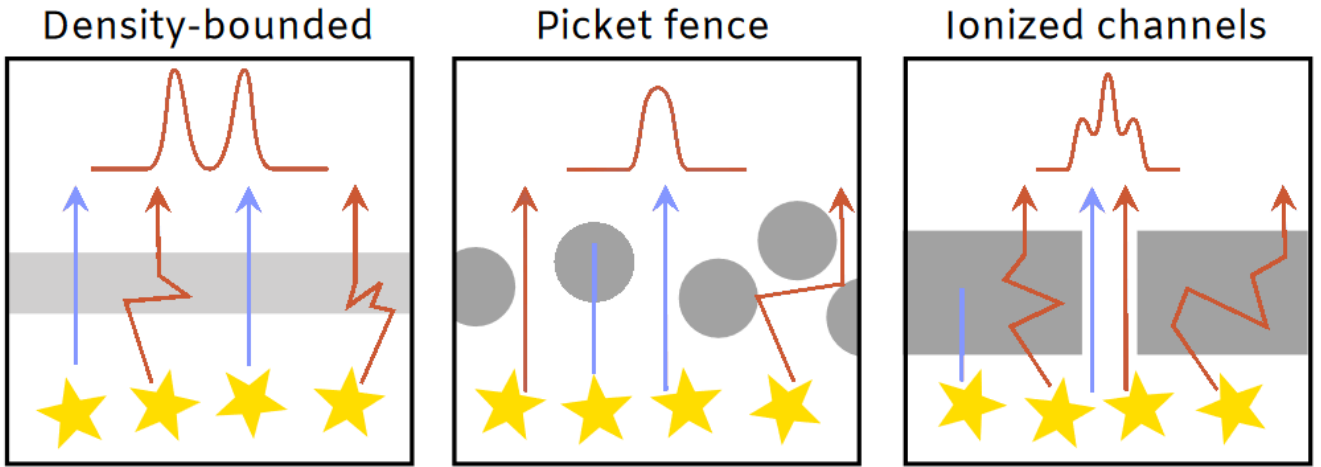


Figure 6: Figure 1 from Rivera-Thorsen et al. (2017). The red arrows represent Ly α photons while the blue arrows represent LyC photons. The grey areas represent neutral hydrogen. Simplistic versions of the resulting Ly α spectra are shown above each case. **Left:** Density Bounded Escape: Both Ly α and LyC photons can escape due to low densities of neutral hydrogen. **Middle:** Clouds of dense neutral hydrogen block some paths of LyC but not all. Ly α can escape directly or by scattering off the clouds. **Right:** LyC photons have ionized a channel through a dense cloud of neutral hydrogen, and there are enough to keep it ionized. LyC and Ly α can escape directly through this channel. Ly α can also escape by scattering within the cloud of neutral hydrogen.

how Ly α scattering leads to spatially extended Ly α the effect of Doppler Shifts changes the spectral line profile.

One often sees multiple separate peaks in Ly α spectra. These are created by Ly α photons being Doppler shifted by neutral gas in the ISM both blueward and redward relative to us. A common, albeit simplistic, model for Ly α escape is the expanding shell model. This model contains a star forming region surrounded by a spherical shell of neutral hydrogen. This shell has an outward velocity (due to stellar winds, supernovae, etc.) which Doppler shifts any Ly α scattering off of it. With enough scattering events, the wavelength of a Ly α photon will be shifted far away from scattering resonance. When this happens, the Ly α photon then can more easily escape, leading to two peaks around the

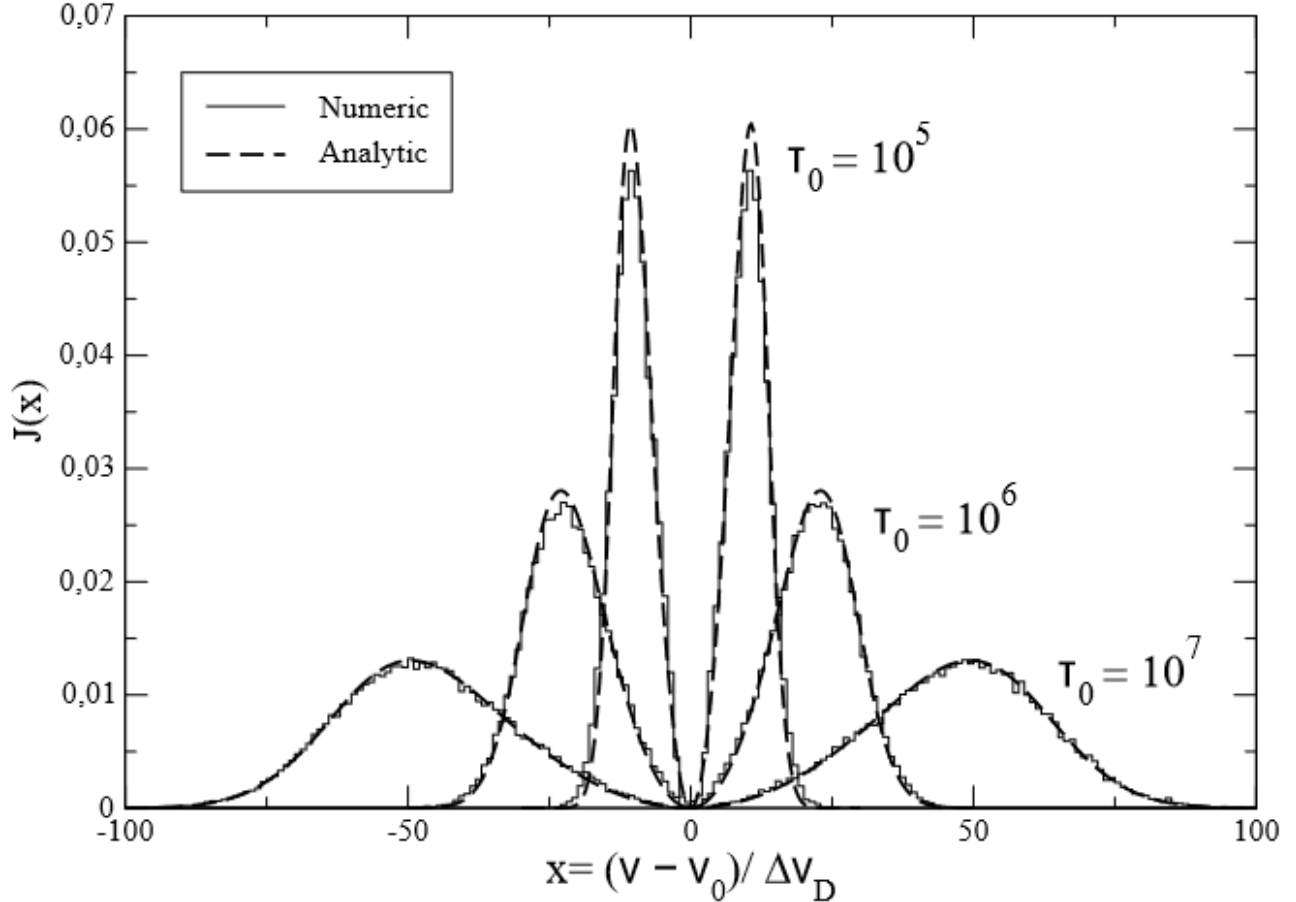


Figure 7: Figure 1 from Semelin et al. (2007). The resulting Ly α spectra from a uniform and spherical cloud of gas at a temperature $T = 10\text{K}$. Three separate distributions are shown and labeled with varying parameter τ_0 : the optical depth at the Ly α line center. The numeric counts are generated by the LICORICE codebase and agree well with analytic predictions for this scenario.

intrinsic Ly α line center. Figure 7 shows the output of LICORICE: a Ly α radiative transfer code that here is simulating an expanding shell model scenario. For each value of the parameter τ_0 —the Ly α line center optical depth—it outputs a double-peaked Ly α spectrum.

However, we know from the previous subsubsection that real neutral hydrogen distributions are not as ideal as a spherical expanding shell. Gronke et al. (2017) uses a similar radiative transfer code (`tlac`, Gronke & Dijkstra (2014)) to simulate Ly α in a clumpy medium. They simulate Ly α traversing through a region filled with spherical clumps of neutral hydrogen at a constant column density

$N_{\text{HI,clump}} = 10^{17} \text{ cm}^{-2}$. The medium is otherwise empty. They control the density of the clumps through the covering factor parameter f_c : the average amount of clumps per sightline. Figure 8 shows the resulting spectra for multiple values of f_c . One can see that as f_c increases, the double peaked shape of Ly α emerges. An increased value of f_c results in a higher density of clumps, and a higher probability that Ly α photons scatter multiple times. Each time Ly α scatters, it is Doppler shifted further away from the intrinsic Ly α line center. It makes sense that the spectra in Figure 8 with high f_c also have high peak separations. Indeed, the same reasoning applies to Figure 7, where increasing optical depth implies more scattering events, leading to Ly α to being shifted farther away from resonance.

Since gas in star-forming regions is not typically moving at relativistic speeds, a single interaction between a Ly α photon and a hydrogen atom can only Doppler shift its wavelength by a small amount. Small Ly α peak separations indicate that many of the escaping Ly α photons did not scatter many times. Since the number of scattering events is dependent on the density of neutral hydrogen, small peak separations imply escape paths with low densities. And since LyC and Ly α are attenuated by the same neutral hydrogen, LyC would preferentially escape along these same routes. Indeed, looking for LyC escape in galaxies with small Ly α peak separation is a tool used by modern astronomers today (Verhamme et al. 2017).

Figure 9 shows a more realistic cartoon of a star forming region and the possible paths Ly α and LyC take. It also shows how different paths result in different Ly α line profiles. The bottom plot in Figure 9 shows the special case of triple-peaked emission profile. It contains two outer peaks corresponding to Doppler shifted Ly α and has a central peak corresponding with a path of direct escape. The figure was developed to explain the configuration of a LyC-leaking clump adjacent to a non-leaking clump in the Starburst Arc: one of the brightest strongly-lensed objects on the sky (Rivera-Thorsen et al. 2017).

1.4. Ly α and LAEs

Young, massive stars in regions of neutral hydrogen (HI regions) produce Ly α in abundance. To first order, these stars ionize their surroundings, creating regions of ionized hydrogen (HII regions).

Static clumps with $N_{\text{HI, cl}} = 10^{17} \text{ cm}^{-2}$

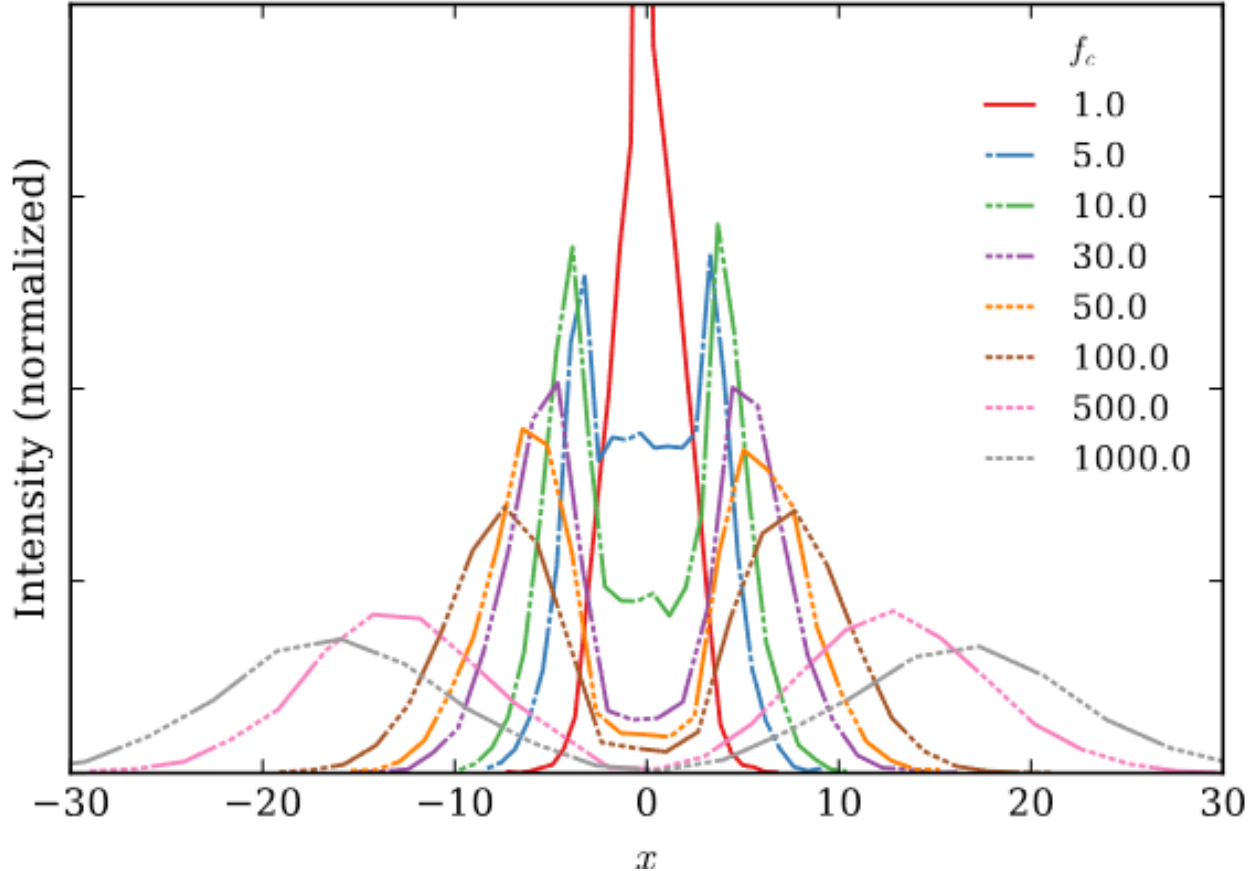


Figure 8: Figure 3 from Gronke et al. (2017). The resulting Ly α spectra escaping from a clumpy medium. Here x represents the Doppler parameter: a measure of how far a frequency has shifted in terms of the intrinsic thermal line width. The clumps have a constant column density $N_{\text{HI,clump}} = 10^{17} \text{ cm}^{-2}$ in an otherwise empty medium. The parameter f_c is the coverage factor, and describes the average number of clumps along a sightline. As the covering factor increases, the double peaked Ly α line structure emerges. These simulations were performed by the code `t1ac` (Gronke & Dijkstra 2014).

At the boundary of the H I and H II regions the ionization rate and recombination rate balance out. As recombination happens, the electron cascades down to the ground state, with a likelihood of $\approx 68\%$ to create a Ly α photon. The specific value of 68% assumes Case B recombination and a temperature of 10^4 K: both valid assumptions for a normal star forming region. However, the temperature of

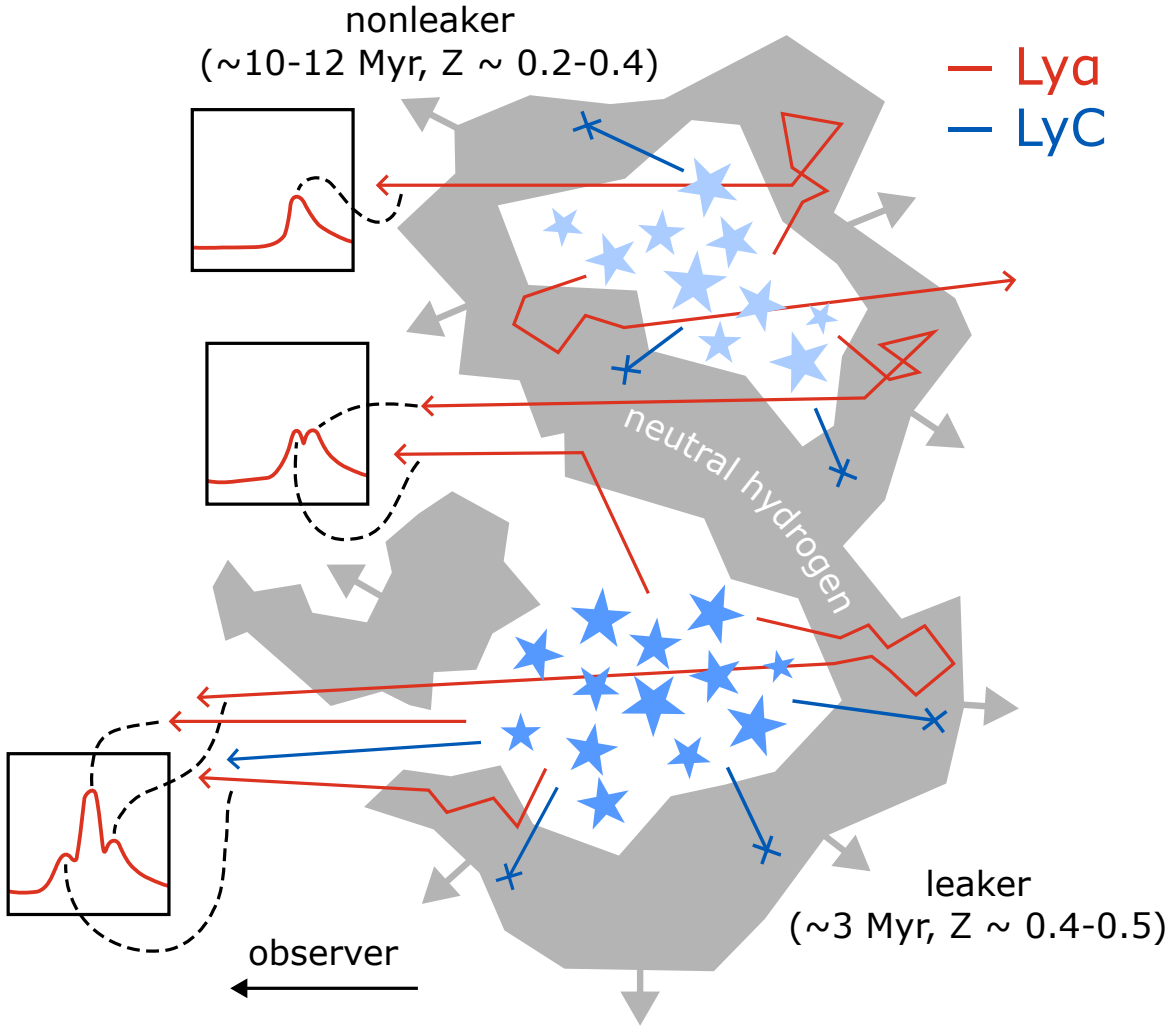


Figure 9: This is Figure 7 from Owens et al. (in prep.). The authors have graciously allowed use of this figure in this work since theirs is currently in preparation. One can see $\text{Ly}\alpha$ scattering within the cloud of neutral hydrogen before escaping. In some cases $\text{Ly}\alpha$ photons scatter many times resulting in a total Doppler shift out of resonance. In these cases the red arrows will continue through an area of neutral hydrogen without interacting. Note that the only LyC photon that escapes does so through a path that $\text{Ly}\alpha$ also escapes through. The plots on the left show how lines of sight to this galaxy capture different sets of $\text{Ly}\alpha$ photons that accumulate into different spectra. The top two plots show 1 or 2 Doppler shifted peaks, and the bottom plot shows two Doppler shifted peaks and a directly escaping peak in the middle.

the gas does affect this probability. It ranges from $\approx 0.8 - 0.6$ for case B or $\approx 0.6 - 0.15$ for case A recombination on a temperature scale of 100K - 10^6 K Dijkstra (2017). This probability can be thought of as an effective conversion factor, which locally converts ionizing photons into Ly α photons. Although, it is important to note that other mechanisms, such as collisional excitation, contribute smaller amounts of Ly α production within these environments.

The stars responsible for creating the majority of the Ly α photons are the most massive: O and B stars. These stars have very high luminosities and short lifespans. The lifetime of an O star is ~ 10 Myr, and a B star is ~ 100 Myr. While these are very long on human timescales, these stars live and die quickly on cosmological timescales. Because of this one can infer that galaxies with significant Ly α emission have young stellar populations, and could actively be undergoing star formation. Similarly, observation of large amounts of Ly α implies that there is not an abundance of dust in the galaxy, which would otherwise attenuate the Ly α flux (Scarlata et al. 2009; Henry et al. 2015; Saldana-Lopez et al. 2023).

A class of galaxies exists which emit significant amounts of Ly α (Cowie & Hu 1998). These galaxies are called Ly α Emitters (LAEs), and are typically classified as having some minimum Ly α EW. This minimum EW is often related to the detection thresholds of the narrowband imaging surveys used to identify samples of LAEs. There is no obvious consensus in the literature on a single Ly α EW threshold, though $\text{EW} \gtrsim 20$ Å is perhaps the most common. Our sample all have Ly α EW > 15 Å, which is very similar (albeit slightly below) the most common literature selection criteria. LAEs are thought to be young and actively star-forming with low to moderate dust content (Gronwall et al. 2007; Finkelstein et al. 2008; Ouchi et al. 2008).

1.5. LAE Morphology

LAEs are typical targets for high-redshift galaxy studies because of their excess brightness in narrowband imaging. Many LAEs have been found at low (Deharveng et al. 2008; Cowie et al. 2011; Östlin et al. 2014) and high redshifts (Cowie & Hu 1998; Rhoads et al. 2000; Yamada et al. 2005; Ouchi et al. 2008; Marques-Chaves et al. 2017; Mukae et al. 2020; Kikuta et al. 2023), suggesting that they are galaxies in a specific stage of evolution, thought to be the progenitors of Milky Way type

galaxies in the local universe (Ono et al. 2010; Dressler et al. 2011; Guaita et al. 2011). However, the astrophysical mechanisms that differentiate this stage are not well understood at high redshifts.

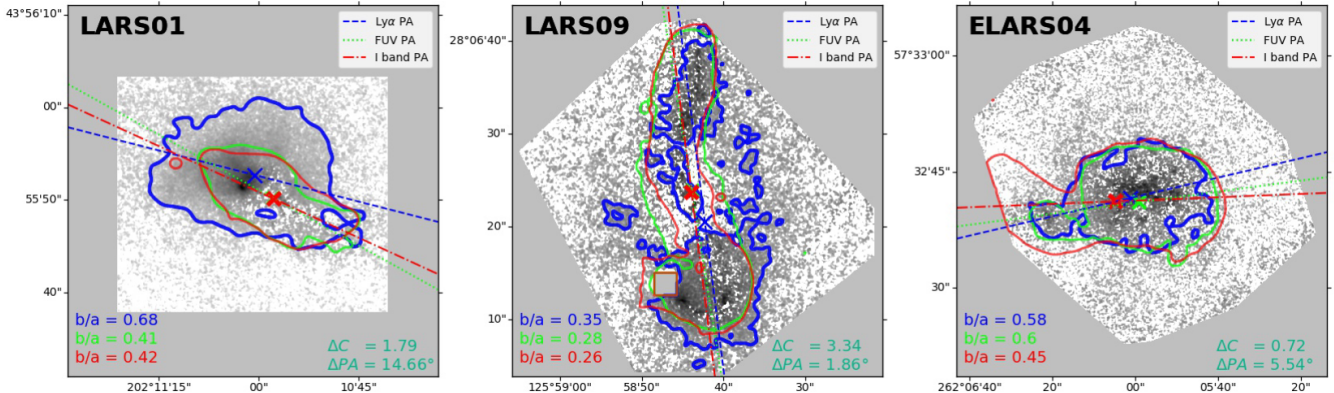


Figure 10: Figure 3 from Rasekh et al. (2022). Three LARS LAEs with brightness contours and morphological parameters. The solid contours represent the Ly α (blue), FUV (yellow), and I-band (red) surface brightness cutoffs. The cutoffs values were chosen as values corresponding with the faintest encompassing isophotes. The grayscale images are Ly α maps constructed from HST imaging data; described in Östlin et al. (2014). The other markings represent morphological parameters, and are beyond the scope of the discussion here.

Narrowband Ly α imaging of LAEs shows heterogeneous morphologies with a range of extents. In local universe LARS LAEs Guaita et al. (2015) finds UV (containing Ly α) half-light radii ($r_{1/2}$) of 0.6 - 12.2 kpc, with 10/12 of their sample < 3 kpc. Only one LAE is found to have UV emission extended beyond the associated optical continuum. Isophotal fitting of a larger sample of LARS galaxies by Rasekh et al. (2022) finds Ly α core scale lengths of 0.11 - 1.59 kpc. A mix of extents are found, with examples of Ly α emission being smaller, consistent with, and larger than the associated FUV. A sample of $0.1 < z < 0.35$ Green Peas studied in Yang et al. (2017); Kim et al. (2021) are found to have Ly α spatial profiles with FWHM 1.5-7.2 times larger than their UV continuum profiles. Steidel et al. (2011) finds an average Ly α scale length of 25.5 kpc in a stack of 52 LAEs at $1.8 < z < 3.4$; $\langle z \rangle = 2.65$. The associated average continuum scale length is 3.1 kpc. Bond et al. (2010) finds that a sample of 7 LAEs at $z = 3.1$ have narrowband Ly α half light radii of

$1 < r_{1/2} < 2.25$ kpc, with FUV continuum $r_{1/2} \lesssim 1$ kpc. In a sample of 3 $z = 4.4$ LAEs, Finkelstein et al. (2011) finds the Ly α $r_{1/2} \approx 1.1$ kpc, each consistent with or extended beyond the associated continuum. Jung et al. (2023) finds evidence of extended Ly α emission for a $z = 7.5$ LAE, with Gaussian $\sigma_{Ly\alpha} = 2.1 \pm 0.4$ kpc, $\sigma_{UV} \approx 1.2$ kpc. Overall, previous studies of LAEs from both the local universe and high-redshift universe appear to show a bimodality in Ly α morphology. Many LAEs have compact Ly α emission on sub-galactic scales, few have Ly α emission consistent with the stellar continuum, and many others have significantly extended Ly α emission larger than the stellar continuum.

As a visual example, I include Figure 10: a subset of the local universe LARS LAEs from Rasekh et al. (2022). While a lot of information is communicated via this figure, the most important feature for our discussion is the solid contours. The background grayscale image is a map of Ly α with contours overlaid. The blue contour corresponds with Ly α , the yellow with FUV, and the red with I-band imaging. One can see that LARS01 has a Ly α contour extended beyond the stellar continuum from the FUV and I-band. LARS09 and ELARS04, on the other hand, have FUV and I-band contours that are similar to or extended beyond the Ly α .

As shown in a simulation of a high-redshift LAE by Blaizot et al. (2023), Ly α luminosity is strongly correlated with gas flows. They find that outflow phases produce bright Ly α lines with strong red peaks, while inflow phases produce faint Ly α lines with strong blue peaks. It is possible that LAEs during outflow phases are more likely to have extended emission, as supernova feedback creates gaps in the ISM neutral hydrogen. Conversely, it is also possible that during inflow phases the fainter Ly α emission is more likely to appear clumpier as gaps are less likely or less pronounced.

Recent studies with JWST and MUSE have shown the importance of faint LAEs to cosmic reionization. Thai et al. (2023) finds an abundance of faint LAEs at high redshift, and Atek et al. (2023) finds that faint high-redshift LAEs have very high ionizing photon production efficiencies. This suggests that LAEs contribute more than previously thought to cosmic reionization. Witstok et al. (2023) finds that their sample of spectroscopically-confirmed LAEs at $z > 7$ are alone not sufficient to produce the ionized bubble sizes inferred from their spectra. They suggest that ultra-faint ($M_{UV} \gtrsim -18$)

LAEs likely play an important role in carving out these bubbles. Herrero Alonso et al. (2023) finds that undetected (presumably faint) LAEs could dominate excess surface brightness seen at large scales in Ly α halos. Magnification from gravitational lensing will be an essential tool to study these very faint LAEs during the EoR.

1.6. *Gravitational Lensing*

Gravitational Lensing is an astrophysical phenomenon wherein very massive objects (e.g. large galaxies or galaxy clusters) warp spacetime. Geodesics—the paths photons take—in warped spacetime appear bent to far away observers. Consequently, light that traversed a region of warped spacetime appears distorted and magnified when projected on the sky. The strength of the effects from lensing are dependent on the geometry of the lens relative to the background source and the mass distribution of the lensing object(s). Certain geometric configurations of background source and foreground lens can create multiple images of the same object or entire rings of light known as Einstein Rings. This is known as strong gravitational lensing. (Wambsganss 1998)

The most important quantity to understand for this work is the angle α (see Figure 11), which determines how to transform an object between the image plane and source plane. The source plane is the plane of the sky at the source and the image plane is the plane of the sky at the observer. The image plane contains the observed, distorted images of the source object, while the source plane contains those images undisturbed. Applying the transformation encoded into α maps is equivalent to ray-tracing an image through the lensing potential. α is calculated by the following equation:

$$\vec{\alpha}(\vec{\theta}) = \frac{1}{\pi} \int \frac{(\vec{\theta} - \vec{\theta}') \kappa(\vec{\theta}')}{|\vec{\theta} - \vec{\theta}'|^2} d^2 \vec{\theta}' \quad (8)$$

where κ is defined as:

$$\kappa(\vec{\theta}') = \frac{\Sigma(\vec{\theta}')}{\Sigma_{critical}} \quad (9)$$

with Σ being the surface density on the sky and the critical surface density defined by:

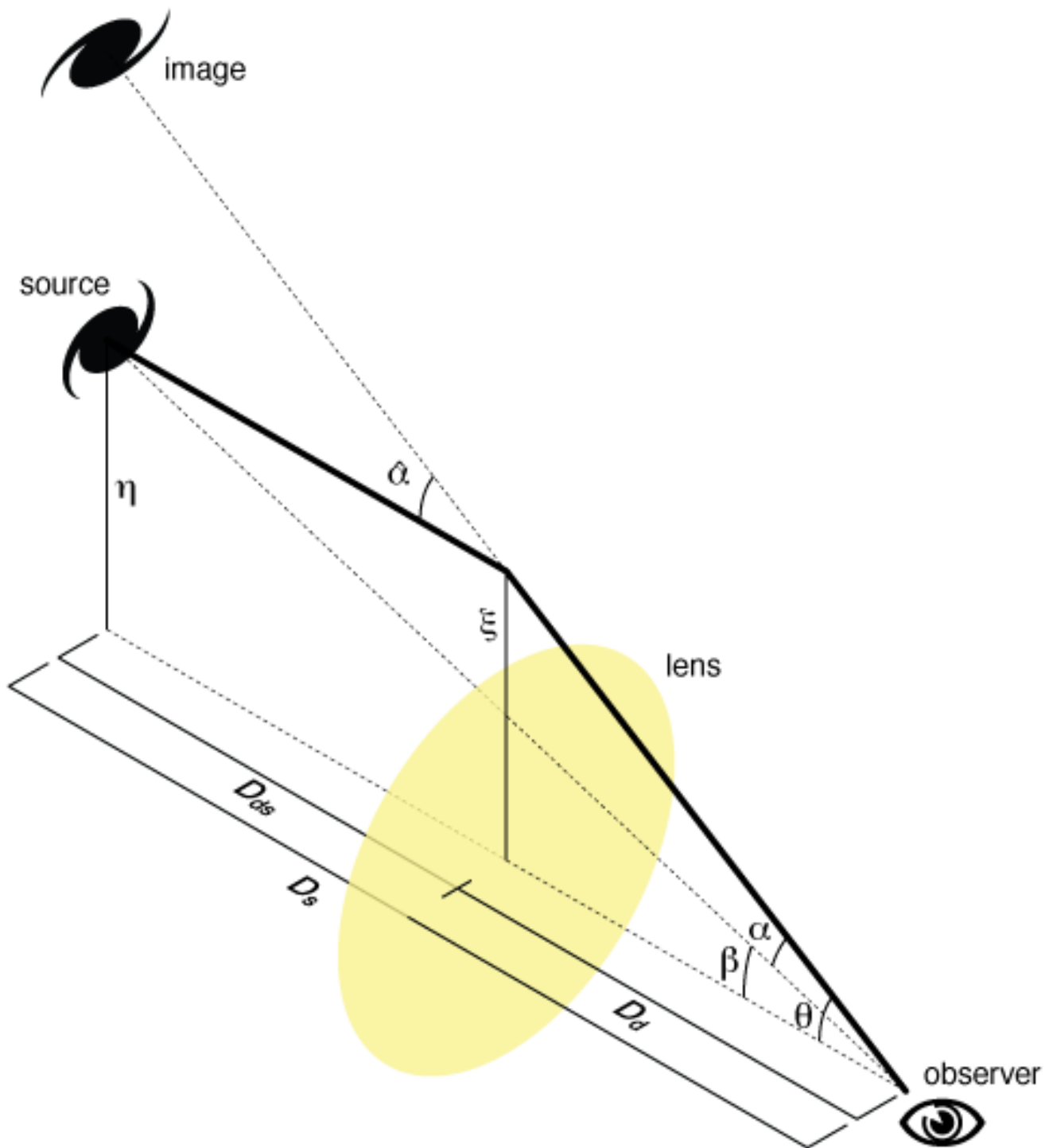


Figure 11: A simplistic diagram of the geometry of gravitational lensing, and the relevant parameters. The bold line represents the path light takes from the object to the observer. Credit for this image is given to Michael Sachs under the CC BY-SA 3.0 Deed license. No changes were made to this image.

$$\Sigma_{critcal} = \frac{c^2 D_s}{4\pi G D_{ds} D_d} \quad (10)$$

Gravitational Lensing is one of astronomers most powerful tools for studying high-redshift galaxies. Gravitational lensing is an achromatic phenomena, meaning that all wavelengths of light on a specific path are deflected in the same way. If one invokes energy conservation, this requires that gravitational lensing conserves the surface brightness of the lensed object. A lensed image of a galaxy will have an increased angular size on the sky from distortion. This increased size directly corresponds to an increase in the total observed flux, as more photons are bent towards our detectors compared to the case without lensing. This allows astronomers to detect intrinsically faint galaxies that modern telescopes would not be able to detect on practical timescales. Additionally, the spatial magnification allows astronomers to probe physical scales that otherwise wouldn't be available at high redshifts. In extreme cases gravitational lensing can even allow for study of single stars; a physical scale otherwise inaccessible outside the local universe (Welch et al. 2022).

* * *

The goal of this thesis is to characterize a sample of high-redshift, gravitationally-lensed LAEs imaged by the Hubble Space Telescope (HST) and Spitzer Space Telescopes. We measure their stellar mass, age, and dust content (A_V), gaining context on the environment in which the Ly α emitting regions exist. We also measure the Ly α flux and luminosity in both the image plane (observed, magnified) and source plane (intrinsic, demagnified). These measurements, in conjunction with previously measured Ly α equivalent widths, show the strength of the Ly α emission. Finally, we show preliminary results of our forward modeling code on one of our LAEs. This code estimates galaxy morphologies in a rigorous way by taking lensing distortions into account.

This paper is organized as follows: in section 2 we introduce our sample of LAEs and summarize the data used. In section 3 we describe our methodologies and measurements. In section 4 we analyze our measurements and discuss our findings. Throughout this paper we assume a Λ CDM cosmology with $(H_0, \Omega_m, \Omega_\Lambda) = (67.7 \text{ kms}^{-1} \text{ Mpc}^{-1}, 0.31, 0.69)$.

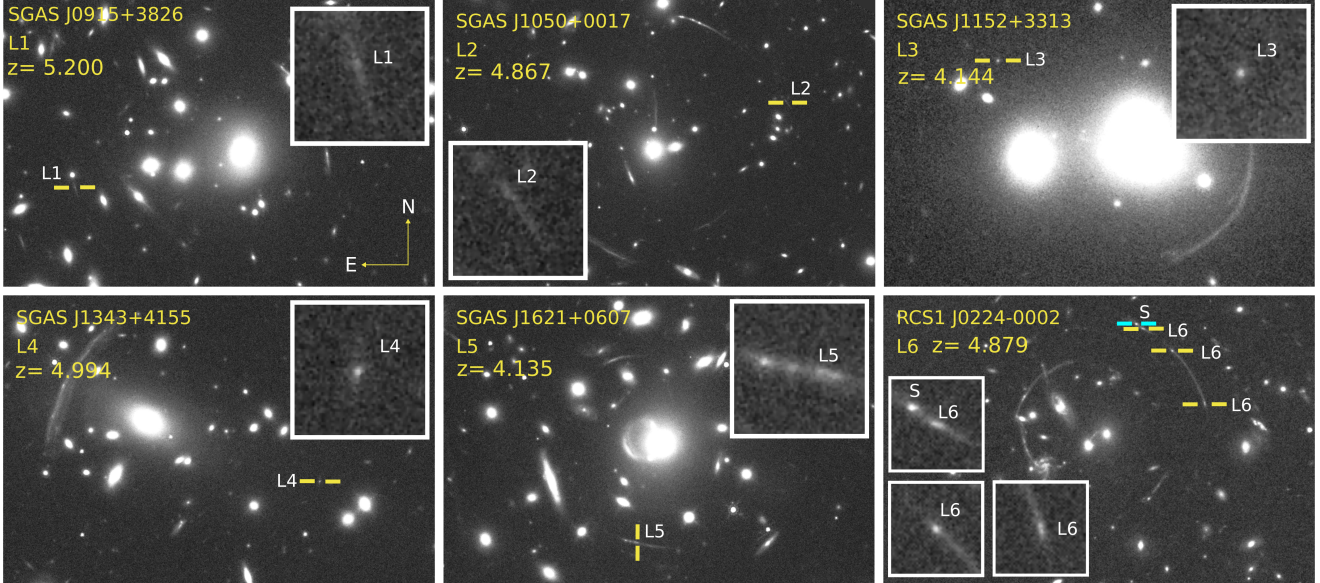


Figure 12: The LAE sample and lensing galaxy clusters. In the cluster view we show F160W (F814W for L6) with the LAEs located by sets of yellow bars. In the postage stamps, close up views of the LAEs are shown in the bluest available filter redward of Ly α that does not contain Ly α . These filters are reported in Table 6 and capture light from the stellar continuum. L6 contains three bright, separated images. A bright galaxy is seen projected onto L6, which we label S and indicate with a set of cyan bars. This galaxy is not gravitationally lensed nor part of L6, but is instead a foreground $z = 3.66$ galaxy (identified by Swinbank et al. (2007)) that serendipitously appears to be part of the arc.

2. DATA

2.1. Lensed LAE Sample

We analyze a sample of six high-redshift ($z > 4$) LAEs. These six lensed LAEs are in the redshift range $4.1 < z < 5.2$. All six have published, well-constrained strong lensing models (Rzepecki et al. 2007; Swinbank et al. 2007; Bayliss et al. 2010, 2014; Smit et al. 2017; Sharon et al. 2020), allowing for spatial analysis at resolutions otherwise inaccessible at these redshifts. Previous studies such as Marques-Chaves et al. (2017); Berg et al. (2018); Erb et al. (2019) have shown the utility of

Identifier	Lensing Cluster	Cluster	LAE	Cluster	Cluster	LAE	LAE
		Redshift	Redshift	RA	Dec	RA	Dec
L1a	SGAS J091541+382655	0.396	5.200	09:15:39	+38:26:59	09:15:41.0	+38:26:53.2
L1b	–	–	–	–	–	09:15:41.0	+38:26:52.3
L2a	SGAS J105038+001715	0.593	4.867	10:50:40	+00:17:07	10:50:38.3	+00:17:14.9
L2b	–	–	–	–	–	10:50:38.4	+00:17:15.2
L3	SGAS J115201+331347	0.517	4.144	11:52:00	+09:30:15	11:52:01.0	+33:13:48.2
L4	SGAS J134331+415455	0.418	4.994	13:43:33	+41:55:04	13:43:30.7	+41:54:55.1
L5	SGAS J162132+060705	0.343	4.135	16:21:32	+06:07:20	16:21:32.6	+06:07:05.6
L6'	RCS1 J022434-000220	0.773	4.879	02:24:34	-00:02:31	02:24:33.8	-00:02:17.8
L6''	–	–	–	–	–	02:24:33.6	-00:02:20.5
L6'''	–	–	–	–	–	02:24:33.3	-00:02:26.9

Table 1: Positions and redshifts of lensed LAEs and lensing clusters. ([Gladders et al. 2002](#); [Sharon et al. 2020](#)). Lowercase letters denote bright regions inside a single image, while apostrophes denote different images of the same bright region. See [Section 3.5](#) and [Figure 20](#) for justification for analyzing our LAEs in this manner. Additionally, we investigate only the brightest and/or most isolated images in each case. We refer the reader to [Gladders et al. \(2002\)](#); [Sharon et al. \(2020\)](#) for information on the other lensed images.

lensing magnification in characterizing the properties of Ly α emitting galaxies both in the image plane (observed on the sky) and source plane (what would be observed on the sky without lensing).

All six lensed LAEs have imaging in broadband filters from HST (rest-frame UV) and Spitzer (rest-frame optical), allowing for broad constraints on the stellar population properties in each galaxy. In this paper we present new narrow-band imaging using tuneable ramp filters on HST that isolate Ly α . These filters allow us to directly measure the morphology and spatial extent of the Ly α emission. The

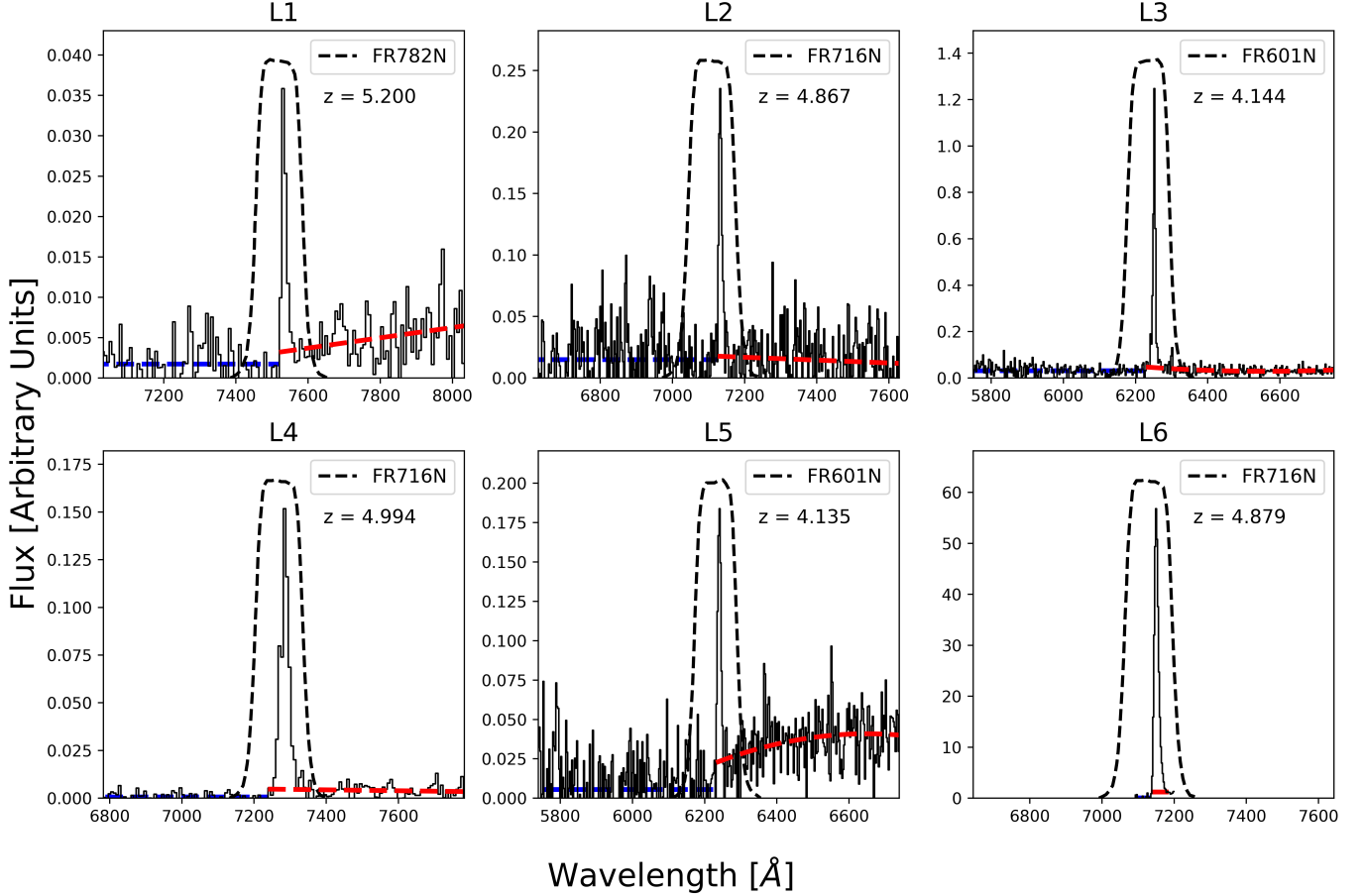


Figure 13: GMOS (L1-L5) and VIMOS IFU (L6) spectra of the LAE sample centered at Ly α . The dashed black curve represents the throughput of the ramp filter used to capture Ly α . The dashed red and blue curves represent linear or quadratic fits to the continuum levels redward and blueward of Ly α . When calculating Ly α fluxes and luminosities we include a multiplicative factor accounting for the fraction of light in the narrowband image coming directly from the Ly α line. The ramp filter properties can be found in Table 2.

individual sources and imaging data sets are described in more detail below. For ease of reference, our sample of six LAEs will be referred to as L1–L6, as shown in Figure 12 and Tables 1 & 4.

2.2. Sample Discovery and Spectroscopic Observations

The sample of strongly lensed Ly α emitting galaxies are drawn from the literature. L6 was first identified in the Red-Sequence Cluster Survey (RCS; Gladders et al. 2003) as a highly extended “giant arc” around a massive galaxy cluster, RCS1 J0224-0002 (see Figure 12). It was found to have a redshift of $z = 4.8786$ based on strong Ly α emission observed with the FORS2 spectrograph on the VLT (Gladders et al. 2002). L6 has been the subject of several detailed studies using ground-based optical and NIR spectroscopy (Swinbank et al. 2007; Smit et al. 2017; Witstok et al. 2021). The spectra of Ly α seen in Figure 13 is from the VIMOS IFU observations from Swinbank et al. (2007), where the IFU covered the entire arc.

ID	Ramp	Ly α	Central	Exposure	Detection
	Filter	[Å]	λ [Å]	Time [s]	Limit [$\times 10^{-16}$]
L1	FR782N	7533.0	7510	7840	1.21
L2	FR716N	7158.4	7134	5060	0.25
L3	FR601N	6249.9	6235	7800	0.33
L4	FR716N	7282.7	7270	5260	0.44
L5	FR601N	6239.0	6230	7700	0.49
L6	FR716N	7142.9	7149	2400	0.53

Table 2: Description of the HST narrowband ramp filter observations. These filters were chosen for their ability to adjust their wavelength coverage. The central wavelengths of the ramp filters were offset to cover the Lyman-Alpha lines seen in the associated Gemini and VLT spectra (see Figure 13). Detection limit refers to the $1-\sigma$ uncertainty in the sky background level within an aperture covering a solid angle of 1 square arcsecond. The detection limit is reported in ergs/s/cm 2 /arcsec 2 .

Telescope	Filter	L1	L2	L3	L4	L5	L6
HST	F160W	23.60 ± 0.02	24.75 ± 0.05	24.60 ± 0.03	24.16 ± 0.02	$21.92 \pm <0.01$	22.43 ± 0.03
–	F125W	23.43 ± 0.02	–	–	–	–	22.56 ± 0.02
–	F110W	–	24.45 ± 0.02	24.58 ± 0.06	–	$21.97 \pm <0.01$	–
–	F105W	–	–	–	24.32 ± 0.03	–	–
HST	F850LP	–	–	–	–	–	22.62 ± 0.08
–	F814W	23.38 ± 0.02	–	–	24.16 ± 0.04	–	21.94 ± 0.01
–	F775W	–	–	–	–	22.10 ± 0.02	–
–	F606W	–	26.01 ± 0.15	24.16 ± 0.03	27.21 ± 0.19	–	23.49 ± 0.02
–	F475W	–	–	25.58 ± 0.10	–	–	–
–	F390W	$< 7.45e-12$	$< 1.64e-12$	–	$< 8.08e-14$	$< 1.28e-11$	–
Spitzer	Ch1	24.32 ± 0.97	23.76 ± 0.19	23.75 ± 0.62	23.51 ± 0.39	20.77 ± 0.02	21.31 ± 0.04
–	Ch2	–	23.85 ± 0.55	$< 1.80e-10$	–	20.89 ± 0.04	22.09 ± 0.13
Ground-Based	i-band	23.34 ± 0.09	–	–	23.78 ± 0.18	–	–
–	z-band	23.39 ± 0.13	–	–	24.24 ± 0.17	–	–

Table 3: Table of Broadband Photometry. We report the AB magnitudes and errors used in our analysis. The italicized entries are considered non-detections, and upper limits are reported in the SDSS unit of maggies to avoid very high AB magnitudes. Maggies are a dimensionless unit defined by: $\frac{f_\nu}{3631\text{Jy}}$. Bold entries are measurements taken from [Bayliss et al. \(2010\)](#). All other entries were calculated in this work.

L1-5 are all located in strong lensing cluster fields found in the Sloan Digital Sky Survey (SDSS; [York et al. 2000](#)) (see [Figure 12](#)). The sources were identified as g- or r-band dropout galaxies in *gri* imaging from the GMOS-N instrument on the Gemini-North telescope. Redshifts for all these sources were measured from strong Ly α emission in follow-up spectroscopy with GMOS-N ([Bayliss et al. 2010, 2011, 2014](#)). The slits in these observations covered the integrated emission from individual images of each LAE. The redshifts for all six LAEs appear in [Table 1](#)

		Observed				Intrinsic		
ID	Ly α	UV M ₁₅₀₀	Ly α Flux [$\times 10^{-18}$]	Ly α Luminosity [$\times 10^{41}$]	Magnification Factor μ	UV M ₁₅₀₀	Ly α Flux [$\times 10^{-18}$]	Ly α Luminosity [$\times 10^{41}$]
	EW [Å]							
L1	25	-25.1	17.9 ± 7.6	53.3 ± 22.7	50 ± 17	-20.9 ± 0.4	0.4 ± 0.2	1.1 ± 0.6
L2	61	-24.0	5.5 ± 0.9	13.9 ± 2.3	12.2 ± 0.7	-21.3 ± 0.06	0.4 ± 0.1	1.1 ± 0.2
L3	65	-23.4	141.3 ± 1.3	247.0 ± 2.4	72.4 ± 9.8	-18.7 ± 0.1	2.0 ± 0.3	3.4 ± 0.5
L4	122	-24.0	90.2 ± 2.0	244.5 ± 5.6	13.0 ± 0.1	-21.2 ± 0.01	6.9 ± 0.2	18.8 ± 0.5
L5	15	-25.9	29.5 ± 2.0	51.3 ± 3.5	46.1 ± 2.7	-21.7 ± 0.06	0.6 ± 0.1	1.1 ± 0.1
L6	120	-25.7	24.5 ± 2.3	62.9 ± 5.9	17.2 ± 16.0	-22.6 ± 1.0	1.4 ± 1.3	3.7 ± 3.4

Table 4: Overview of our sample’s UV and Ly α properties. The objects’ rest-frame Ly α equivalent width are taken from Gladders et al. (2002) and Bayliss et al. (2011, 2014). The ultraviolet absolute magnitudes were calculated from our best-fit SED models. The Ly α fluxes and luminosities were calculated from the HST narrowband filter imaging following the methodology reported in Section 3.1. We report the flux in ergs/s/cm². We report the luminosities in ergs/s. The magnifications were calculated from the lens models of each system. We note that L5 has an Ly α EW of 15, slightly below the common Ly α EW threshold of 20. We include it in our sample due to its large observed Ly α flux and high signal-to-noise.

2.3. *HST Narrow-band Imaging*

We obtained narrow-band imaging isolating Ly α for each object in our sample taken with the narrow-band ramp filters installed on Hubble’s Advanced Camera for Surveys (ACS). The reduced science images are available on the Harvard Dataverse Navarre (2023a, 10.7910/DVN/9Q0YYW). These filters are tunable, allowing for coverage of precise wavelength ranges. We obtained these data as part of HST guest observer (GO) program #13639 (PI: Bayliss). Each ramp filter provides an image with a narrow bandwidth ($\Delta\lambda/\lambda \simeq 2\%$) over a field of view covering approximately $\approx 40'' \times 60''$

on the sky. Each source received between 1 and 3 orbits of ramp filter observations ($\sim 2400 - 7800$ s total integration time). We list the ramp filter used, the tuned central wavelength, and exposure time for each lensed LAE in Table 2. Figure 13 shows the spectra of all six lensed LAEs centered on Ly α with the transmission curves of the ramp filters used to isolate Ly α for each source. We reduced The ACS ramp filter data following standard procedures using Drizzlepac¹ (Gonzaga et al. 2012). We drizzled the exposures taken in each filter using the `astrodrizzle` routine with a Gaussian kernel and a drop size of `final_pixfrac` = 0.8. We combined them to a common world coordinate system (WCS) using `tweakreg` and `tweakback`, and co-added them with `astrodrizzle` onto a common reference grid with North up and a pixel scale of $0.^{\prime\prime}03 \text{ px}^{-1}$. The final reduced narrowband images for each LAE are background limited.

2.4. *Broadband Imaging*

We also analyze broadband imaging of each of our lensed LAEs from several different observatories, spanning the optical through infra-red. For L1 and L4 we use i- and z-band magnitudes measured with the GMOS-N instrument on the Gemini-North telescope and published by Bayliss et al. (2010). We measure additional broadband imaging photometry from HST and Spitzer data for all six lensed LAEs.

2.4.1. *HST*

Five of our lensed LAEs—L1 through L5—were imaged with the Wide Field Camera 3 (WFC3) on the Hubble Space Telescope using both the IR and UVIS channels as a part of HST GO program # 13003 (PI: Gladders). In short, each field was observed in two UVIS broadbands—one of [F814W, F775W, F606W], and one of [F475W, F390W]—and in two IR broadbands—F160W and one of [F125W, F110W, F105W]. L4 is a slight exception, as it has UVIS imaging only in F390W, as well as imaging from Hubble’s Wide Field Planetary Camera 2 (WFPC2) in F606W and F814W that was

¹ <http://www.stsci.edu/scientific-community/software/drizzlepac.html>

taken as a part of HST GO program # 11974 (PI: Allam). All of these observations are described in [Sharon et al. \(2020\)](#), and we use the same reductions described there.

L6 has HST imaging from several different programs, all of which we incorporate into our analysis. The available data include: WFPC2/F814W (13200 s) and WFPC2/F606W (6600 s) obtained by GO # 9135 (PI: Gladders), ACS/F850LP (1949 s) obtained by GO # 13639 (PI: Bayliss), and ACS/F814W (8046 s), WFC3-IR/F125W (12486 s), and WFC3-IR/F160W (15369 s) from GO # 14497 (PI: Smit). We reduced these data using the same procedure that was applied to the ACS ramp filter data described above. For a more detailed description of the reduction methods see [Sharon et al. \(2020\)](#).

The available broadband data ([Sharon, Keren 2022](#)) allows us to fit spectral energy distributions with multiple points over a broad wavelength range for our entire sample, always with at least two HST broadband filters that sample the stellar continuum emission redward (and uncontaminated by Ly α).

2.4.2. *Spitzer*

Our lensed LAE sample has rest-frame optical broadband imaging available from observations taken with the Infrared Array Camera (IRAC) on the Spitzer Space Telescope. The reduced science images are available on the Harvard Dataverse ([Navarre 2023b](#), 10.7910/DVN/JSVGM8). For sources L1 - L5 we have IRAC imaging in Channel 1 (Ch1; $\sim 3.6\mu\text{m}$) and Channel 2 (Ch2; $\sim 4.5\mu\text{m}$) taken as a part of programs # 60158 (PI: Gladders), # 70154 (PI: Gladders), and # 90232 (PI: Rigby). For L6 we have IRAC imaging in Ch1, Ch2, Channel 3 (Ch3; $\sim 5.8\mu\text{m}$), and Channel 4 (Ch4; $\sim 8\mu\text{m}$), taken as a part of program # 20754 (PI: Ellingson). Ultimately we only use the Ch1 and Ch2 data of L6 in our analysis because the combination of larger IRAC point spread functions (PSF) and higher backgrounds in Ch3 and Ch4 prevent us from meaningfully constraining the flux in those bands. The L6 Spitzer imaging was reduced with the same procedure as described in section 3.2 of [Florian et al. \(2021\)](#) with AOR 15102976. The Spitzer data sample the rest-frame $\sim 6000\text{-}9000\text{\AA}$ spectra of our lensed sources.

To correct the small coordinate offset ($\sim 1''$) between the HST and Spitzer data, we used Source Extractor (Bertin & Arnouts 1996) catalogs of the HST and Spitzer imaging to match positions of bright objects in the fields, and registered the data set onto the same WCS reference frame.

3. METHODOLOGY

3.1. *Photometry*

AB magnitudes were measured in every available broadband filter, and are shown in Table 3. The photometry was performed using elliptical apertures that match well to isophotal contours of the LAEs. We then applied PSF-dependent encircled energy (HST) and aperture correction (Spitzer) calibrations in each band to avoid aperture-based color effects. These calibrations serve to correct the amount of flux observed in an aperture. Point-Spread Functions (PSFs), as their name suggests, spread out point sources of light into extended shapes. The shape of the PSF depends on the (imperfect) geometry of the telescope and optical systems, and the size depends on wavelength and size of the primary mirror. In the ideal case of a circular mirror being diffraction limited, the angular resolution is:

$$\theta = 1.22 \frac{\lambda}{D} \quad (11)$$

where λ is the wavelength being observed and D is the diameter of the mirror. To account for PSF-broadened light falling outside your chosen aperture, these calibrations are calculated. As an example, Figure 14 shows the encircled energy (EE) curves for filters used in the Hubble Space Telescope UVIS instrument. As the name suggests, these are the percentages of total energy contained within circular apertures of different radii. To achieve correct fluxes, one simply divides their observed flux within their aperture by the EE value corresponding with their aperture radius and filter.

When determining the calibration values with elliptical apertures, we treated the minor axis as an effective radius. Distortion from gravitational lensing occurs along an angular path, with which we aligned the major axis of our elliptical apertures. The less distorted radial direction is thus aligned with the minor axis, and better represents the true angular size of the image.

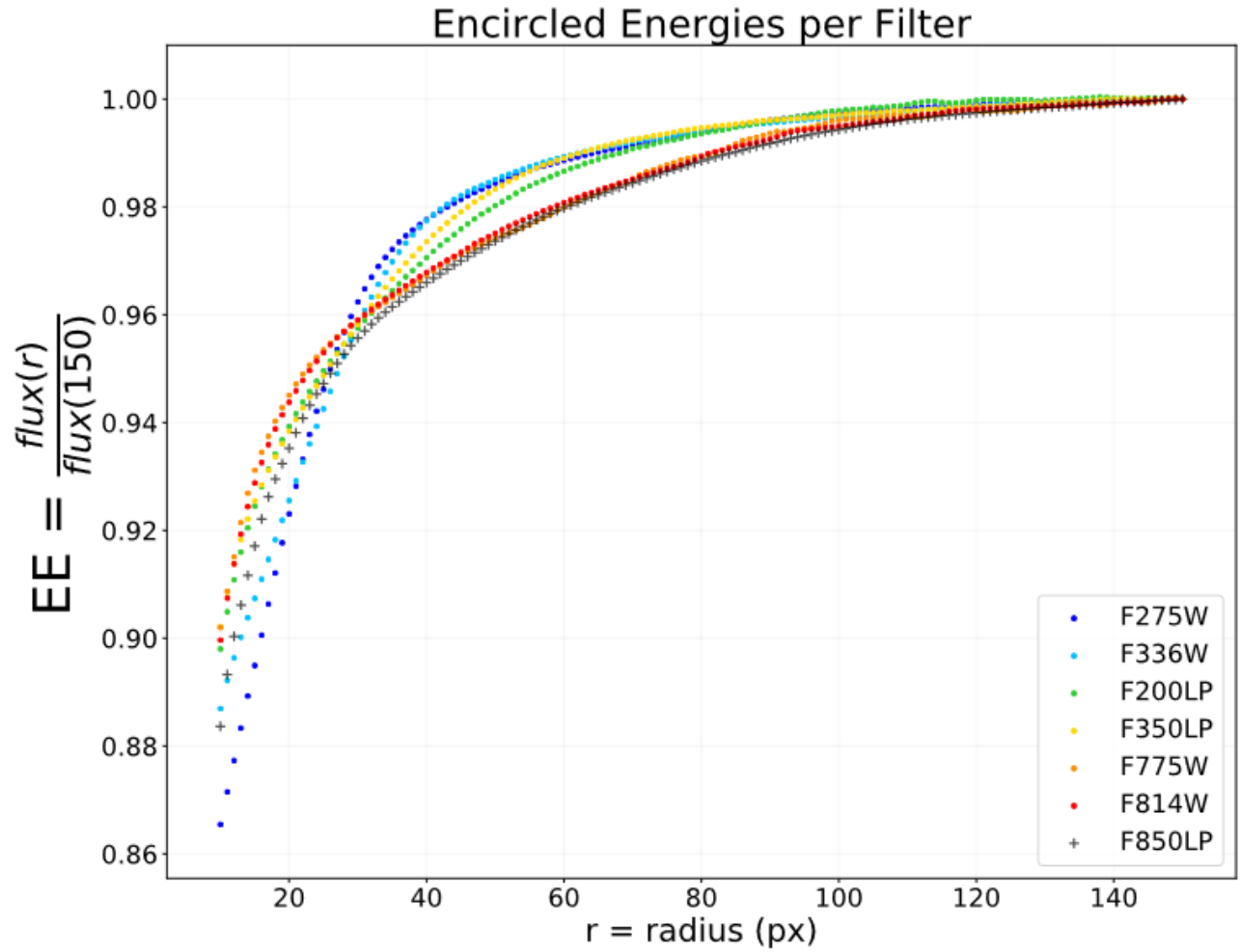


Figure 14: Figure 9 from Medina et al. (2022). Measurements of the encircled energy (EE) for a wide range of filters used by HST-UVIS. The shapes of the EE curves differ between bands because the shapes of the PSF also differ between bands. In the limiting case of large radii, all EE curves approach 100% enclosed energy, as expected.

We estimated the error in the photometry as a combination of the background noise and poisson noise. To obtain the background noise we took measurements of the blank sky nearby each LAE, masking out bright sources. The standard deviations of these pixel sets were taken as the background noise in each pixel. The total background noise was then $\sqrt{N} * \sigma_{sky}$, where N is the number of pixels within the photometric aperture. The Poisson noise was calculated as $\sqrt{N_e}$ where N_e is the

(background subtracted) number of electrons measured within the photometric aperture. These errors were summed in quadrature to obtain the total error reported.

We report the narrowband Ly α flux and luminosity in [Table 4](#). The Ly α flux density was calculated in the same manner as the broadband photometry described above. The total flux was calculated by multiplying the flux density by the bandwidth of the narrowband filter it was observed in. We remove the continuum contribution to the narrowband flux for each object. We do this by fitting the continuum both redward and blueward of Ly α using linear or quadratic polynomials depending on the shape of the continuum (see [Figure 13](#)). We then use the continuum fit to directly compute the fraction of the total integrated flux in each narrowband filter that results from the continuum vs. line emission. We compute the Ly α luminosity from the continuum-subtracted Ly α flux and the cosmological luminosity distance at the LAE redshift. We do not use the Ly α photometry in our SED modeling because `Prospector` does not rigorously model Ly α radiative transfer ([Section 1.3](#)).

Multiple imaging refers to when one lensed object has multiple known images. For objects in our sample that were multiply imaged we analyzed only a subset, preferentially choosing the brightest and/or most isolated. The chosen images are the ones indicated by the yellow bars in [Figure 12](#). L1, L2, L3, and L5 have multiple images, but only one was bright enough and isolated enough from other nearby bright sources. L4, while highly magnified, is not multiply imaged. L6 has three bright, isolated images. Our photometry of L6 is a combination of all its images, as they are not separable in the Spitzer imaging.

It is visually obvious from the panel containing L5 in [Figure 12](#) that the image contains three bright regions. However, only one of these regions contains Ly α (the westernmost region, see [Figure 20](#)). Like L6, our photometry of L5 is a combination of all three regions because they are not separable in the Spitzer imaging. However, our offset measurements ([Section 3.5](#)) consider only the region containing Ly α .

Many of the LAEs in our sample have significantly brighter neighboring sources which could in principle contaminate the photometry. This is especially a concern in the Spitzer data as Spitzer pixels and PSF are large compared to the LAE sizes and the HST PSF, leading to blending of

sources. To correct for this, the software GALFIT (Peng et al. 2010) was used to subtract out the bright nearby sources. GALFIT is a software developed to model galaxy morphologies based on imaging data. The GALFIT models were Sérsics, 2D Gaussians, or a linear combination of the two. The equation for a (centered) Gaussian is:

$$f(r) = A \exp\left(\frac{-r^2}{2\sigma^2}\right) \quad (12)$$

where A is the amplitude and σ is the standard deviation. The equation for a (centered) Sérsic is:

$$f(r) = I_e \exp\left(-b_n \left[\left(\frac{r}{r_e}\right)^{1/n} - 1\right]\right) \quad (13)$$

where r_e is the half-light radius: the radius which contains half of the light of the distribution. I_e is defined as the surface brightness at r_e , and n is the Sérsic index; a free parameter. b_n is a constant that satisfies:

$$\gamma(2n; b_n) = \frac{1}{2}\Gamma(2n) \quad (14)$$

where Γ is the Gamma function, and γ is the lower incomplete Gamma function. b_n is solved for numerically. To create 2D distributions x and y coordinates are mapped onto a generalized ellipse in the following way:

$$r(x, y) = \sqrt{\left(x^2 + \left[\frac{y}{q}\right]^2\right)} \quad (15)$$

where q is the skew parameter. The model is then finally rotated by another free parameter: the position angle.

GALFIT uses a gradient descent minimization algorithm. In each iteration GALFIT creates a model from the supplied parameters and evaluates the goodness of fit. The parameters are changed in the next iteration by evaluating the gradient of the current parameters and moving along that vector in parameter space. GALFIT stops when it finds a stable minimum.

Models of the PSF were empirically created from the available stars in each field and photometric band. The geometric models of the galaxy were convolved with the appropriate PSF model in each iteration of the GALFIT algorithm.

L6 has a bright spot initially believed to be a bright star-forming image of the LAE. However, spectral analysis by [Swinbank et al. \(2007\)](#) shows that it is actually a separate galaxy at a redshift of 3.66 that happens to coincide with the lensed arc. This object is labeled by the cyan bars in Figure 12, and was subtracted using GALFIT before any photometric measurements were performed.

In the Spitzer data where this galaxy is indistinguishable from the LAE, we attempt to subtract it by first galfitting a model to it in F160W. We then transfer the F160W model to the Spitzer data, keeping the position and morphological parameters fixed while allowing the brightness to change.

Our GALFIT models fit the outer regions of galaxies well, but left behind residuals in the cores. However, in most cases these residuals were ignored. Through iterating GALFIT, we were able to build models where the residuals were small and spatially removed enough from our apertures. In a subset of the Spitzer imaging this was not the case, and our apertures contained the imperfect residuals. To combat contamination in these cases we calculated photometry given five GALFIT models with different model parameterization and similarly good quality of fit, then report the average. Particularly in L1-L4, this led to higher uncertainties than due to the sky background alone. L1-L4 are spatially compact and the most susceptible to blending with their bright neighbors. The magnitude of the GALFIT systematic uncertainties was similar to the magnitude of the uncertainty from the sky background in any particular realization. In all cases, the GALFIT residuals are believed to be a consequence of imperfect PSF modeling and/or contamination from intra-cluster light.

3.2. Stellar Population Synthesis Modelling with *Prospector*

We utilize the *Prospector* ([Johnson et al. 2021](#)) framework for Bayesian Spectral Energy Distribution (SED) fitting and stellar population synthesis modeling based on the photometric and spectral measurements reported in this work. *Prospector* utilizes stellar libraries ([Conroy et al. 2009; Conroy & Gunn 2010](#)), and employs Monte-Carlo Markov Chains (MCMC; [Foreman-Mackey et al. 2013](#)) to sample posterior distributions of galaxy parameter spaces.

Like the gradient descent used in GALFIT, the MCMC algorithm is iterative. It uses the *Stretch Move* algorithm, described as follows. There exists a set S of k walkers with positions X_k . Each walker represents a position in parameter space and corresponds one-to-one with a galaxy property such as stellar mass or A_V . Each walker is initialized according to the user-specified prior distributions, the models at their positions are evaluated, and then the positions of the walkers are given proposed updates. The position of a walker X_k is proposed an update like

$$X_k \rightarrow X_k + Z [X_k - X_j] \quad (16)$$

where X_j is a randomly chosen walker with $j \neq k$. Z is a random variable drawn from the distribution

$$g(z) \propto \begin{cases} \frac{1}{\sqrt{z}} & z \in [1/2, 2] \\ 0 & \text{otherwise} \end{cases} \quad (17)$$

Then an intermediate parameter q is calculated

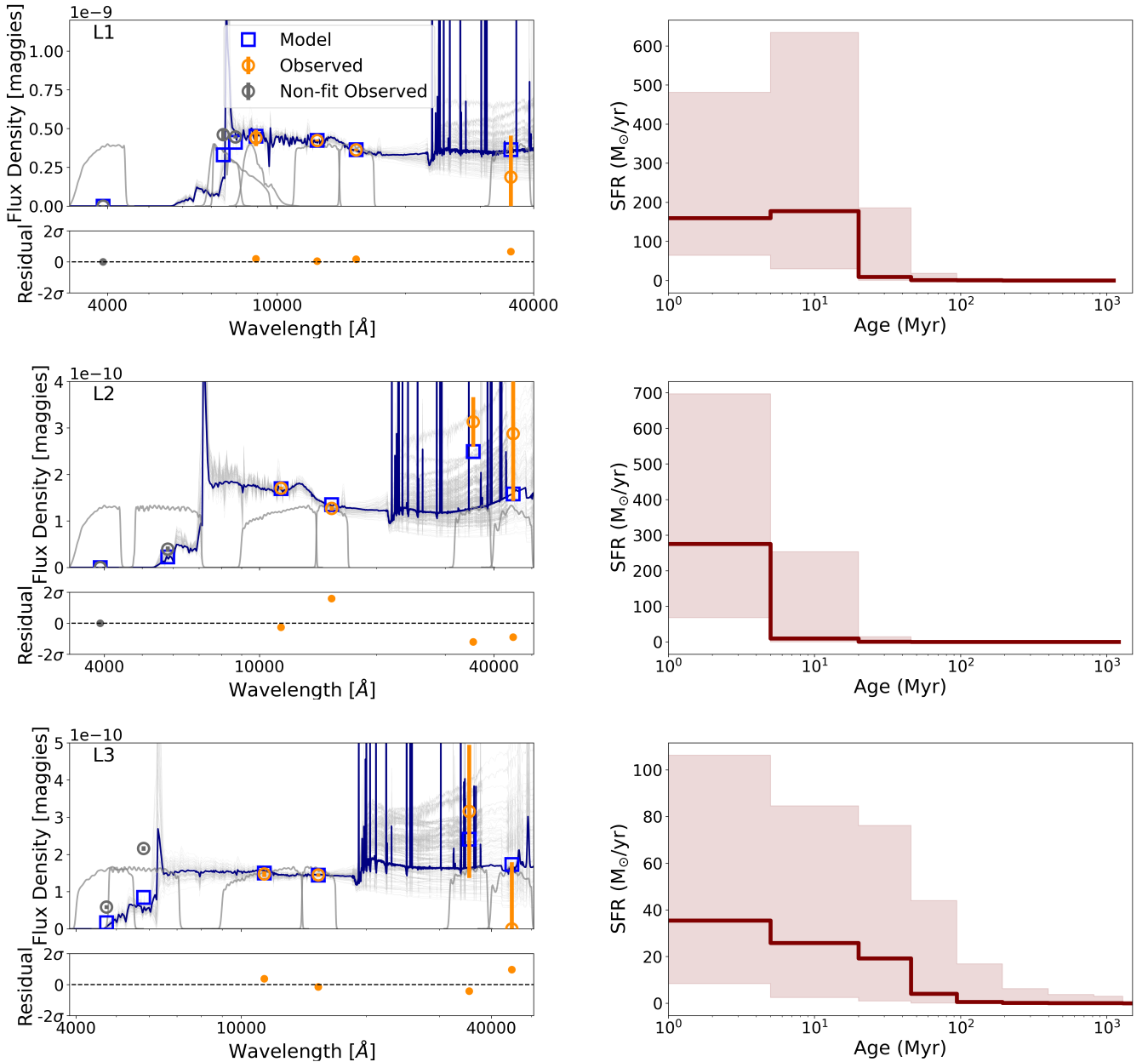
$$q = \min \left(1, Z^{N-1} \frac{p(X_k + Z [X_k - X_j])}{p(X_k)} \right) \quad (18)$$

where N is the dimension of the parameter space and p is the likelihood function. Finally, a continuous random variable, r , between 0 and 1 is generated. If $r \leq q$ then the new walker position is accepted. If not, the walker stays at its current position. In each iteration this happens in series for all walkers.

Use of an MCMC algorithm is very effective at modeling in high-dimensional parameter spaces such as ours. Small proposed steps are more likely to be accepted if near a good solution (local minimum), but big proposed steps can still be accepted. This allows for exploration across the parameter space while focusing on regions with good fits. Using the *Stretch Move* algorithm outperforms the standard Metropolis-Hastings algorithm used in previous SED codes, allowing for significantly shorter run times.

The best fit SEDs for our sample of LAEs are shown in Figure 15. The reported properties and uncertainties are the 16th, 50th, and 84th percentiles of these distributions. These percentiles correspond to the mean and standard deviations of a Gaussian distribution. While the probability distributions sampled by `Prospector` are not necessarily Gaussian, these percentiles still provide a suitable measure of the values and uncertainties.

We ran `Prospector` with a combination of the parametric_sfh, dust_emission, and nebular libraries. These libraries allow us to jointly model stellar mass, stellar metallicity, stellar population



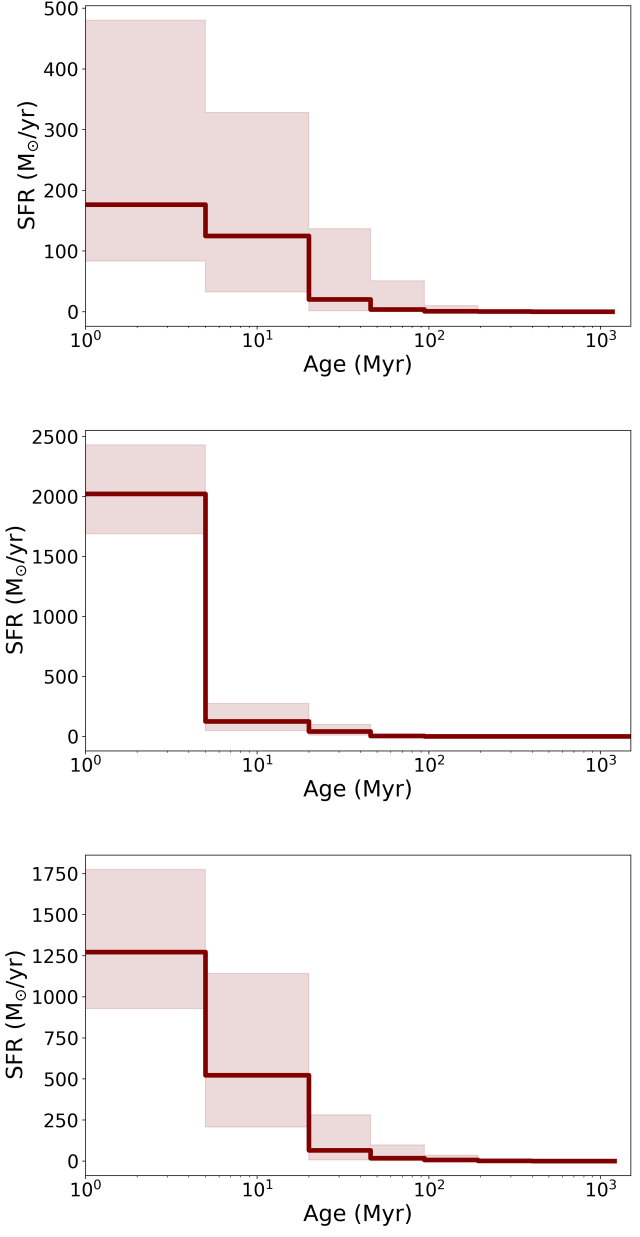
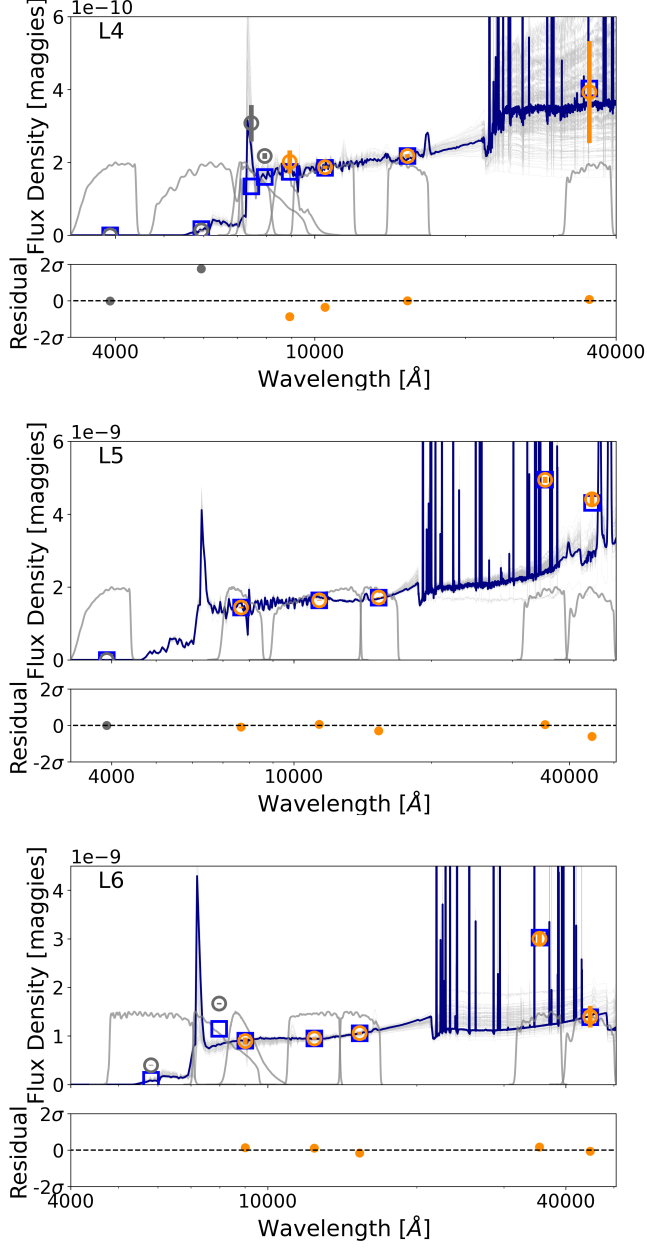


Figure 15: **Left:** SED models. The best fit model for each LAE is shown by the dark blue curve. The gray curves behind the best fit curve are the final 100 iterations from the end of the Emcee chain. These approximate the spread of models **Prospector** fits to the data. Filter transmission curves for our photometry are plotted at the bottom of each plot in gray. They are shifted in wavelength space to match the redshift of the LAE and are aligned with the photometric points. **Right:** Non-parametric star-formation histories. Age is defined as the lookback time from the time we currently see to the age of the universe at the object’s redshift. The line and shaded regions are the 16th, 50th, and 84th percentiles of star formation rate in each age bin. The SFRs are calculated in the image plane and are hence magnified.

age, amount of dust, gas-phase metallicity, and ionization parameter U as free parameters. Metallicity is defined as the amount of non-hydrogen atoms within the stellar population or gas cloud compared to the amount in our sun. The ionization parameter U is the ratio of ionizing photon flux and the gas density. It is defined as:

$$\frac{h}{4\pi r^2 c N_e} \int L_\nu \frac{d\nu}{\nu} \quad (19)$$

where L_ν is a luminosity density, r is the radius of the gas cloud, and N_e is the electron density. However, the constraining power of our photometry only robustly constrained the stellar mass. The amount of dust and age of the stellar population are less constrained, but are reported for context. The stellar and gas phase metallicities and the ionization parameter U were not meaningfully constrained. Redshift was kept fixed in all cases except for L4, which had a strong $H\alpha$ emission line on the edge of the IRAC Channel 1 transmission curve. This was inferred from the brightness of the $\text{Ly}\alpha$ line and the $\text{Ly}\alpha$ -based redshift. We do not have a precise measurement of the true systematic redshift, so in this case we allowed the redshift to vary over a small range calculated using [Verhamme et al. \(2018\)](#): an investigation into offsets between systematic and $\text{Ly}\alpha$ based redshift measurements. The extent to which $H\alpha$ lies under the transmission curve has a large impact on the inferred properties from the fit. Allowing redshift to vary for L4 ensures we are not biased towards only one possible set of parameters. Additionally, we chose to exclude any photometry from bands that contained $\text{Ly}\alpha$ because **Prospector** cannot model $\text{Ly}\alpha$ emission rigorously.

At the redshifts of our sample the HST photometry constrains the UV slope and luminosity of the young stellar populations. The Spitzer/IRAC data sample broad swaths of the rest-frame optical for all of our sources and measures the continuum emission from older stellar populations and nebular emission lines in each lensed LAE. The Spitzer data therefore provide constraints on the strength of the Balmer jump, marginalized over uncertainties in the strengths of the nebular emission lines.

We make use of **Prospector**'s ability to model non-parametric SFHs; we chose a non-parametric SFH with fixed time bins and the continuity prior. As described in [Leja et al. \(2019\)](#), this SFH setup

is the best case scenario for recovering true SFHs with photometry-only SED fitting. We define eight age bins:

$$\begin{aligned} 0 < t \leq 10 \text{ Myr} \\ 10 < t \leq 30 \text{ Myr} \\ 30 < t \leq 60 \text{ Myr} \\ 60 < t \leq 130 \text{ Myr} \\ 130 < t \leq 260 \text{ Myr} \\ 260 < t \leq 550 \text{ Myr} \\ 550 \text{ Myr} < t \leq 1.1 \text{ Gyr} \\ 1.1 \text{ Gyr} < t \leq t_{final} \end{aligned}$$

where t_{final} is the age of the universe at the redshift of the LAE. Except for the first two and last age bins, the age bins are separated equally in logarithmic time, following the methodology of [Leja et al. \(2019\)](#). The first two bins were chosen to probe populations of very young (< 10 Myr and 10-30 Myr old) stars. Each LAE was modeled with 256 walkers and a total of 9216 MCMC iterations, excluding three preliminary "burn-in" runs.

We report three measures of the age of the stellar population: mass-weighted age, t_{50} , and t_{90} . The mass-weighted age is defined as the integral of the SFH weighted by the total amount of mass formed in each time bin. t_{50} and t_{90} are defined as the times at which the (unweighted) integral of the SFH is equal to 50% and 90% of the total stellar mass formed.

The errors on all three quantities are drawn from 1000 realizations of the SFH (1000 different walker/iteration combinations). From these distributions we report the 16th, 50th, and 84th percentiles. It is critical to note that `Prospector` calculates the stellar mass posterior distribution from image plane photometry, which is magnified by strong gravitational lensing. We calculate the intrinsic stellar mass distribution by convolving the posterior with a Gaussian distribution of the object's magnification factor.

ID	Ly α	log(Stellar Mass)	log(Stellar Mass)	Mass-Weighted	t_{50}	t_{90}	Dust1	Dust2
	Morphology	[M_\odot] (Lensed)	[M_\odot] (Intrinsic)	Age [Myr]	[Myr]	[Myr]	[A_V]	[A_V]
L1	Clumpy	$9.85^{+0.62}_{-0.48}$	$8.15^{+0.64}_{-0.51}$	17^{+19}_{-8}	13^{+14}_{-7}	44^{+510}_{-25}	$0.10^{+0.23}_{-0.08}$	$0.82^{+0.92}_{-0.69}$
L2	Clumpy	$9.72^{+0.43}_{-0.61}$	$8.60^{+0.44}_{-0.61}$	8^{+9}_{-3}	4^{+11}_{-1}	18^{+220}_{-13}	$0.09^{+0.14}_{-0.07}$	$2.15^{+0.64}_{-1.30}$
L3	Extended	$9.69^{+0.58}_{-0.68}$	$7.79^{+0.58}_{-0.68}$	33^{+83}_{-20}	38^{+230}_{-26}	187^{+850}_{-150}	$0.57^{+0.84}_{-0.43}$	$0.35^{+0.75}_{-0.29}$
L4	Extended	$9.94^{+0.45}_{-0.40}$	$8.82^{+0.45}_{-0.40}$	20^{+27}_{-9}	17^{+41}_{-7}	87^{+580}_{-68}	$0.46^{+0.47}_{-0.28}$	$0.54^{+0.69}_{-0.39}$
L5	Clumpy	$10.41^{+0.09}_{-0.08}$	$8.71^{+0.10}_{-0.10}$	7^{+2}_{-1}	4^{+1}_{-1}	33^{+12}_{-18}	$0.23^{+0.06}_{-0.06}$	$1.00^{+0.16}_{-0.15}$
L6	Extended	$10.55^{+0.26}_{-0.26}$	$9.24^{+0.47}_{-0.37}$	16^{+11}_{-06}	14^{+26}_{-6}	130^{+490}_{-110}	$0.42^{+0.56}_{-0.31}$	$0.80^{+0.39}_{-0.44}$

Table 5: Table of inferred galaxy properties from `Prospector`. The associated SEDs are found in Figure 15 and correspond with the above quantities. Dust is broken into two components: dust1 and dust2. These are defined as the amount of dust attenuation affecting stars with ages < 10 Myr (dust1) and > 10 Myr (dust2). This distinction is based on the work of Charlot & Fall (2000), where the environments of young and old stellar populations contain different amounts of dust (see Section 4.1). We report three measures of the age: mass-weighted age, t_{50} , and t_{90} , as defined in Section 3.2. We include the Ly α morphology classification (see Section 4.3) for reference.

3.3. Lens Models

Modeling the gravitational potential of the lensing system is an important aspect of analyzing strongly lensed sources. Creation of magnification maps, identification of all the images of a lensed source, and creation of source-plane images through ray tracing are all examples of obtaining information only available through lens modeling. In this work we used magnification maps to calculate the intrinsic stellar mass and intrinsic Ly α magnitudes of our sample. We also identified previously unknown images of L1 and L5, but they were too faint for robust analysis. We leave use of lens models to calculate physical (source plane) sizes and distances for the subsequent paper on this sample Navarre et al. (in prep.).

Lensing models of the systems were created using `Lenstool` (Jullo et al. 2007), which is a parametric lens-modeling software in which projected mass density halos are linearly combined. All models assumed a pseudo-isothermal ellipsoidal mass distribution (PIEMD, Limousin et al. (2007)) with the following parameters: position, ellipticity, position angle, core radius, truncation radius, and normalization. The models are iteratively created; beginning with modeling the most obvious evidence of lensing, then using the output to identify additional constraints.

Lens models for L1 through L5 were computed by Sharon et al. (2020). The lens model for L6 was created for this work. All of the lens model outputs are publicly available through MAST². Here we provide only a short summary, and refer the reader to Sharon et al. (2020) for more details. The details of the lens model of L6 will be presented in Navarre et al. (in prep).

3.4. Forward Modeling of Galaxy Morphology

Morphological modeling of gravitationally lensed galaxies in the image plane is extremely difficult because of the distortion on the sky. Even if a morphological model were well fit to some image plane data, inferring intrinsic galaxy properties from that model would still need to account for lensing effects. Additionally, more distorted galaxies would require more complex/numerous model components, increasing the overall degrees of freedom. This would effectively obscure the intrinsic properties of one galaxy behind many model components. Instead of modeling in the image plane, we developed new python code to model galaxies in the source plane based on the image plane data.

The code works as follows, and is also visually described in Figure 16: First, images of the galaxy in the source plane are created via backwards ray tracing the image-plane data through the lensing potential. As discussed in Section 1.6, the angular quantity that relates positions in the image plane to positions in the source plane is $\vec{\alpha}$. Since alpha is a vector quantity, we need two maps: α_x : the angular displacement along the x-axis at every point and α_y : the angular displacement along the y-axis for every point. Since these transformations take place over very small portions of the sky, we can treat the sky as a flat plane. α_x and α_y serve as a one-to-one mapping between the source plane

² <https://archive.stsci.edu/hlsp/sgas>

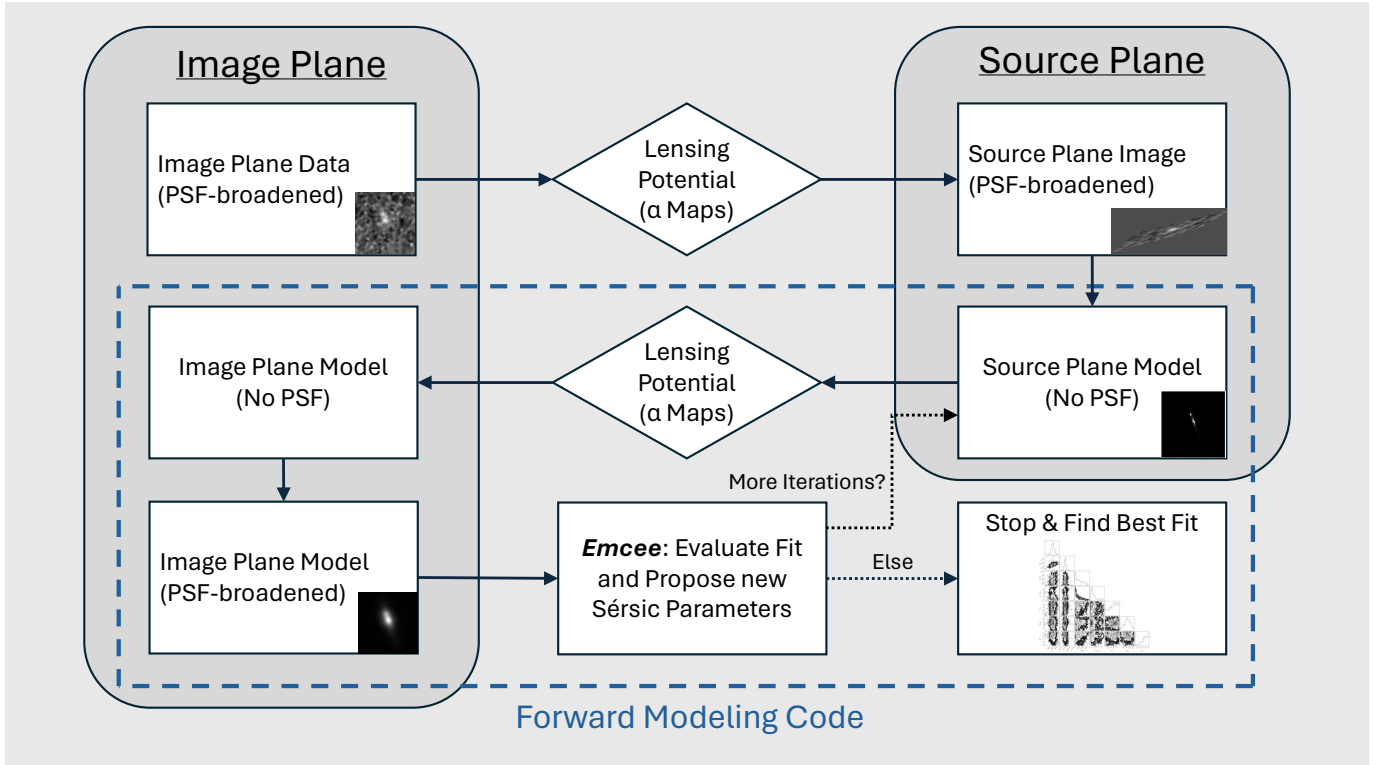


Figure 16: A flowchart description of how the forward modeling code works. Example images of L1 at different steps of the process are shown. The final box contains a smaller version of Figure 17: the posterior distributions of the Sérsic parameters and their correlations. Forward modeling allows one to model galaxy morphologies while taking into account the uncertainties associated with gravitational lensing. See Section 3.4 for a detailed walkthrough.

and image plane. With these maps, we take the corners of image-plane every pixel to the source plane, which distorts them.

To work with these source plane images, we re-sample them onto a finer (square) pixel grid (we chose 1/10 of a native pixel; 0.003''). This choice is called the fine sampling factor, and is arbitrary. The level of detail is defined by the size of the image plane pixels and the lensing distortion. Increasingly smaller pixels will not reveal any additional information, but will cause code run times to increase. Figure 18 shows the re-sampled source-plane image for L1 (further results are located in Section 4.4).

It is important to note that the effects of PSF broadening also translate to the source plane (often being quite distorted), and thus one cannot directly model the intrinsic galaxy morphology from this

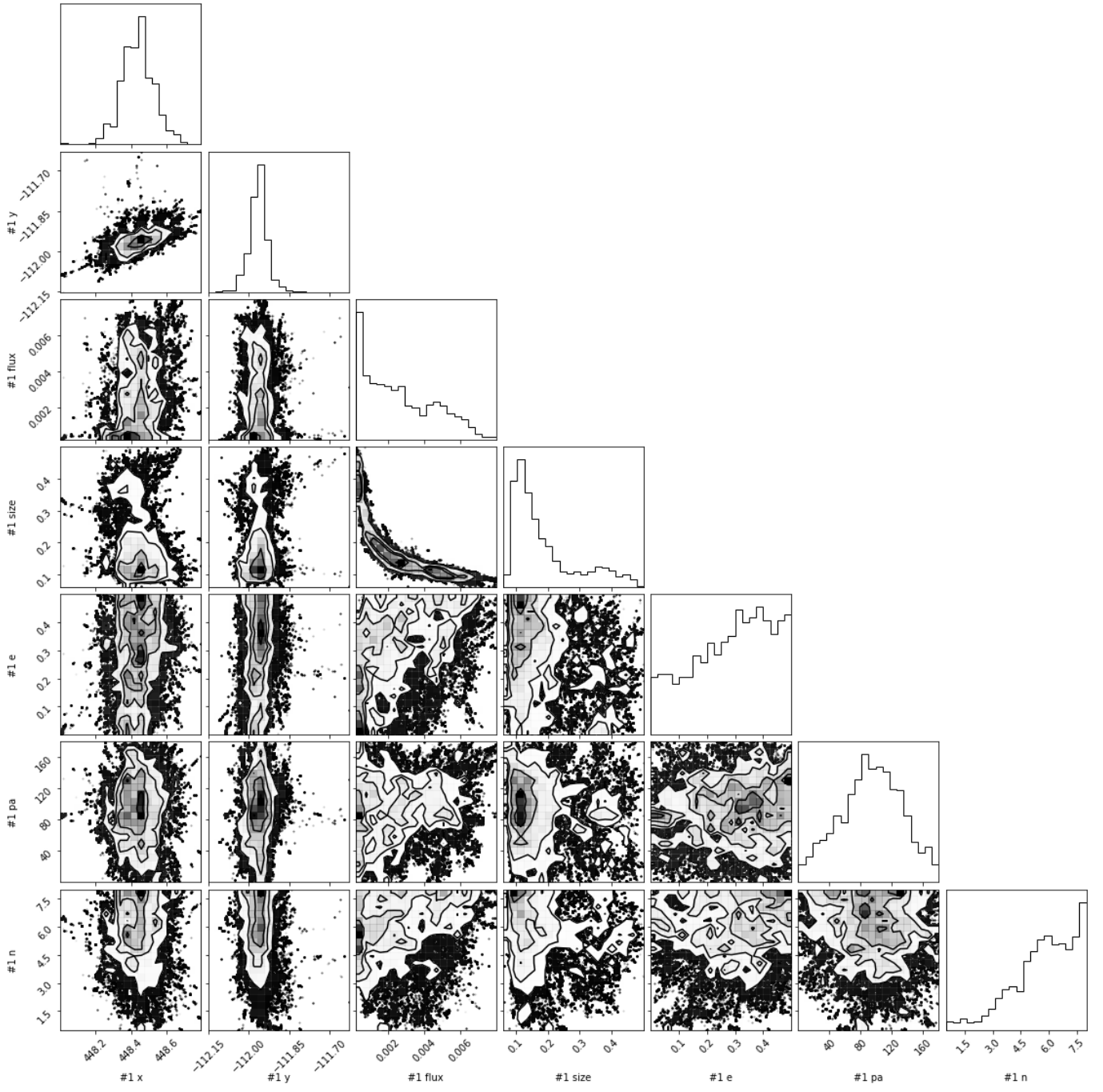


Figure 17: The posterior distribution and correlations for the Sérsic parameters for clump 1 of L1. The diagonal contains the posterior distributions: the probability density of the different parameters. These are built from the positions of the Emcee walkers at each iteration. The inner plots contain the correlation between the two posterior distributions along each inner plot's axes. The uncertainties in the posterior distributions come from the statistical uncertainties of the data, the uncertainties in the lensing model, and the uncertainties due to the PSF broadening.

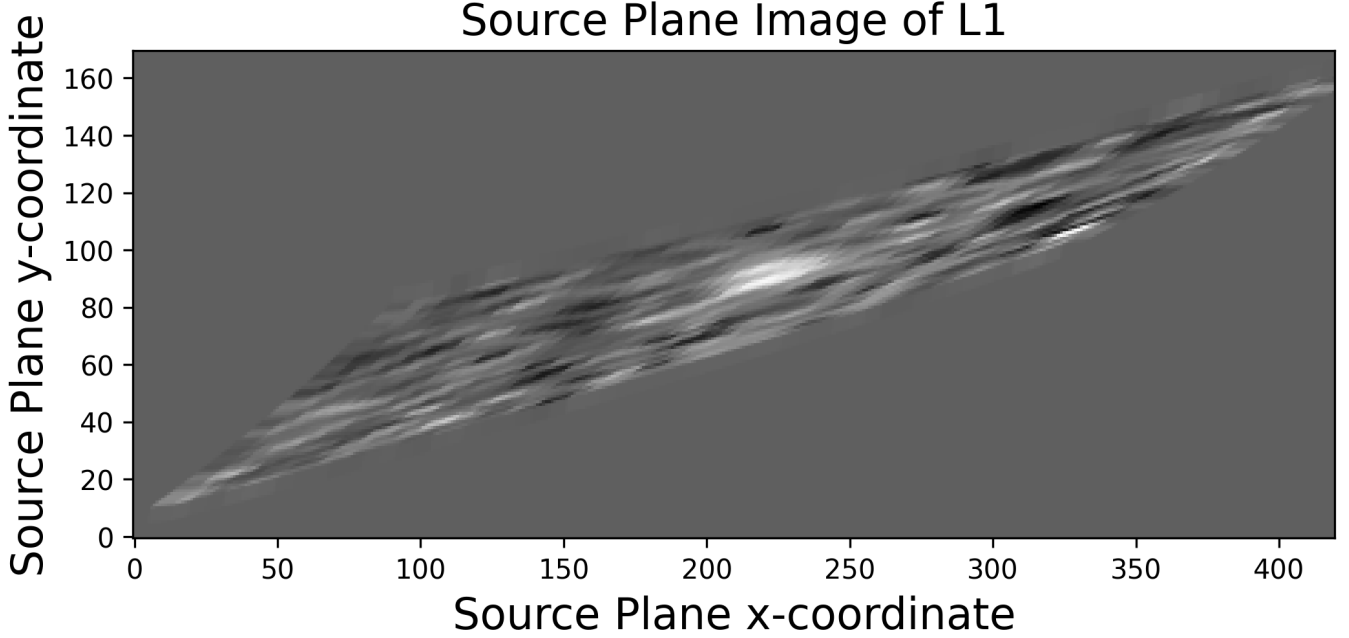


Figure 18: The Source Plane model of L1 in F125W. The image-plane pixels, although resampled onto a 10x finer grid, can still be seen by eye via the rhombus-like patterns. Here we see two peaks of emission, which correspond with the two clumps seen in the image plane. These distributions contain the lensed effects of PSF-broadening.

image. However, one can still gain useful modeling parameters from it. The source-plane centroid positions of the (PSF-broadened) galaxy distributions are unaffected. That is to say that PSF broadening only affects the shape of a source, not its position. Therefore, we can extract the centroid position(s) from the source-plane images to use as the basis of our morphological modeling.

We identify the number of peaks in flux density associated with the galaxy (as opposed to random sky noise) in our source plane image, and record their centroids. For each peak we model a 2D Sérsic profile. Similar to the Sérsic modeling for GALFIT (see Section 3.1), each Sérsic model contains 7 parameters: the center coordinates x and y , the half-light radius $r_{1/2}$, the surface brightness at the effective half light radius I_e , the ellipticity e (equivalent to the skew parameter q in GALFIT), the position angle PA, and the Sérsic index n . These model parameters create 2D distributions, which we plot on a grid with the same fine-sampling factor as the source plane images. We then use the

α maps to transform our model distributions back to the image plane, and resample the resulting distribution back on to an image-plane pixel-size grid.

Once our model is mapped onto an image plane grid, we convolve it with the PSF corresponding to the filter the image was originally taken in. This PSF-convolved model can then be subtracted from the image-plane data, leaving a residual. The residual is evaluated for goodness of fit by comparing the distribution of flux to the separately measured sky-noise distribution. We use Monte-Carlo Markov Chains (Foreman-Mackey et al. 2013, `Emcee`) to iteratively sample the parameter space, repeating the above procedure at every accepted step. The `Emcee` algorithm is what is used in `Prospector` (*Stretch Move*), and the reader is referred to Section 3.2 for more detail.

Although the `Emcee` algorithm is slow, it produces good-fitting models and rigorous constraints on the model parameters (posterior distributions, parameter correlations, etc.). This is especially apparent when you have more than one Sérsic profile being modeled at a time, giving a $7 \times N$ dimensional parameter-space for N Sérsic profiles. Other algorithms like gradient descent do not include these features and do not navigate high-dimensional parameter spaces as well.

3.5. Offset Measurements

Through visual analysis of the stellar continuum and narrowband Ly α imaging, we found separate bright regions within the images of L1, L2, and L5. We denote these regions with lowercase letters (L1a, L2b, etc.). Note these should not be misinterpreted as multiple images of the same object, like those found L6. The positions of each region are shown in Table 1 and can be seen visually by the Xs in Figure 20.

We calculated the on-sky offset between the stellar continuum and Ly α emission of each region of interest. To represent the stellar continuum, we chose the bluest filter available that contained the UV slope and did not contain Ly α . We calculated the on-sky positions by using DS9’s (Joye & Mandel 2003) centroiding algorithm in each band.

ID	Image Plane $\delta_{Ly\alpha}$ ["]	Stellar Continuum Band
L1a	0.090	F125W
L1b	0.042	F125W
L2a	0.067	F110W
L2b	0.030	F110W
L3	0.060	F110W
L4	0.042	F105W
L5	0.030	F775W
L6'	0.095	F850LP
L6''	0.108	F850LP
L6'''	0.095	F850LP

Table 6: Image-plane (on-sky) angular offsets between the stellar continuum and Ly α emission. We list the filters used for the stellar continuum, which were chosen as the bluest available filters redward of Ly α that did not contain Ly α . Since our measurements do not correct for distortion from gravitational lensing, our findings should be considered as upper limits to the intrinsic (source plane) separation.

3.6. Classification of Clumpy vs. Extended

We classify the Ly α morphology of our LAEs in two broad categories: clumpy and extended. This classification is derived from the spatially-resolved ratio of the Ly α emission to the UV continuum emission. Our observations in both Ly α and the UV continuum are background limited, and we interpret their pixel-by-pixel ratio as something akin to a Ly α escape fraction map. The UV continuum is created from the same young, hot stars that create Ly α . Additionally, the ionizing photon emission from these stars should scale with the UV continuum. Assuming a $f_{esc,LyC} \sim 0$, every ionizing photon should result in approximately 0.68 Ly α photons (from Dijkstra (2017)). In some LAEs we see both regions of high Ly α , low UV; and regions of low Ly α , high UV surface brightness. This can be seen

visually in Figure 20. We classify these LAEs as clumpy. We classify the other LAEs as extended, as their Ly α surface brightness scales more smoothly with the UV continuum into the CGM.

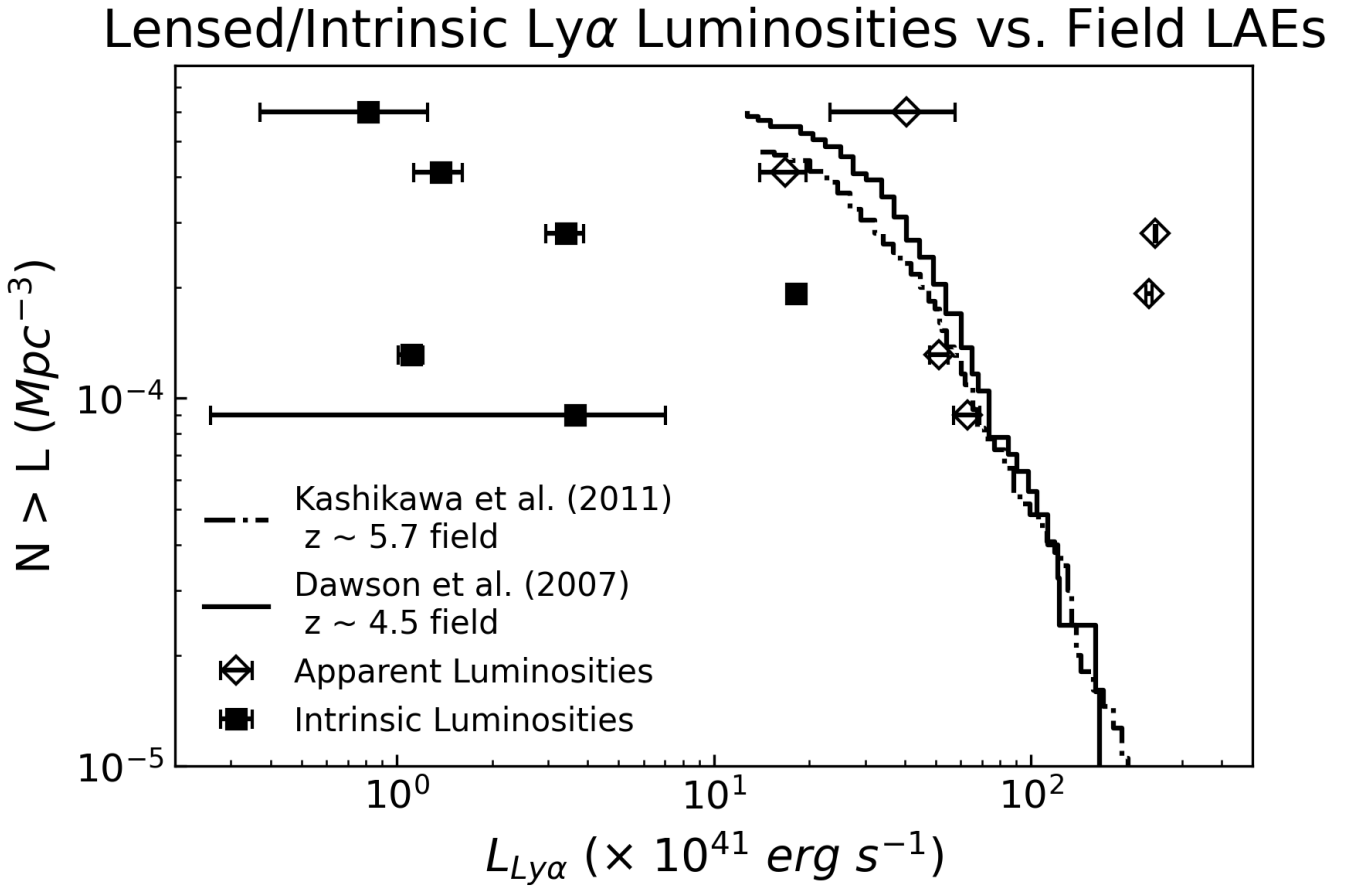


Figure 19: The solid and dashed lines show luminosity densities of high-redshift field LAEs from Kashikawa et al. (2011) and Dawson et al. (2007). The open diamonds are the measured Ly α luminosities of our sample. The filled squares are the intrinsic (delensed) luminosities, calculated from our lens model magnification maps. Note that the y-coordinates of our data points do not represent a number density. The intrinsic and observed luminosities of an LAE are placed at the same y-coordinate for clarity. Our observed luminosities are consistent with or brighter than typical field LAEs at these redshifts. The y-axis ordering of the points corresponds with L1 at the top and descends to L6 at the bottom.

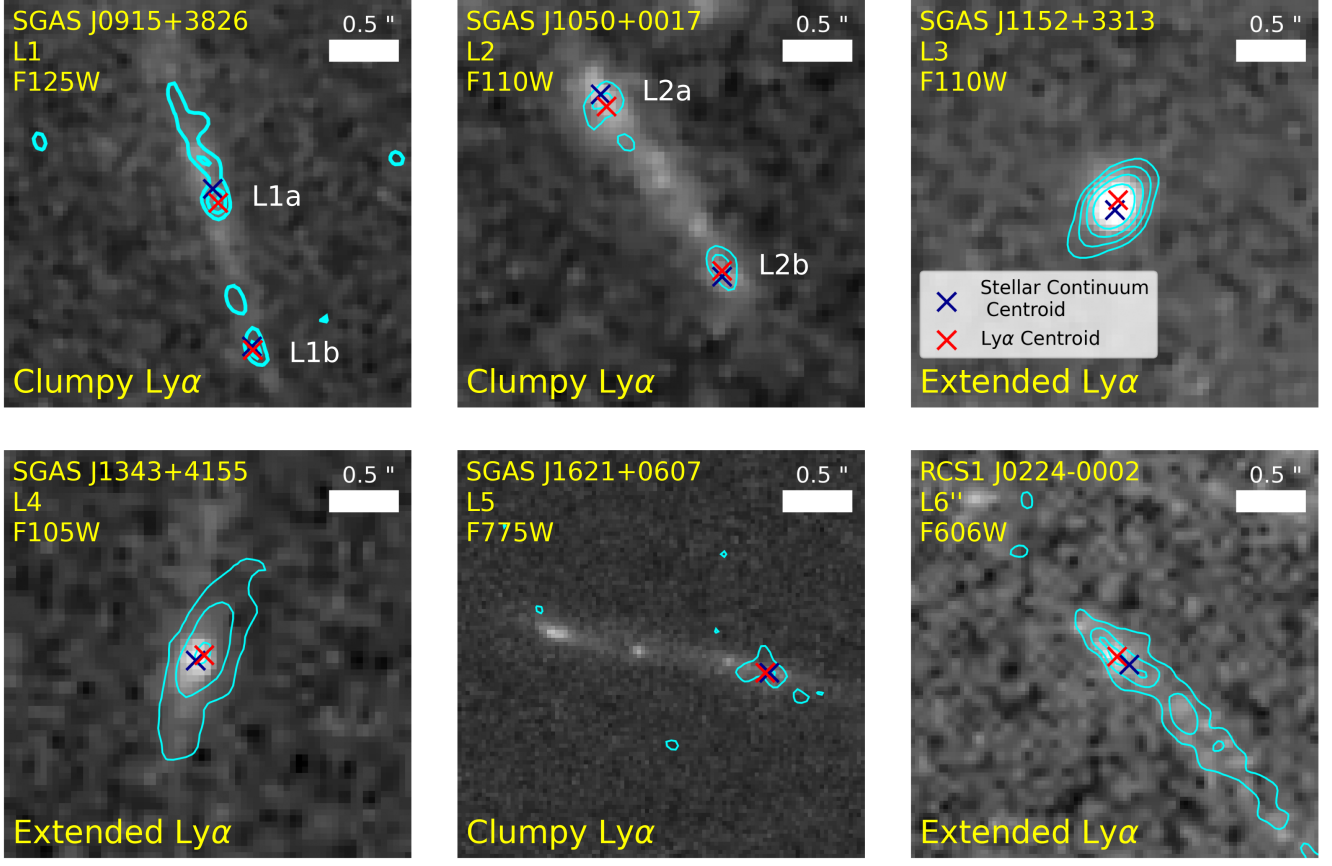


Figure 20: View of the LAE morphologies in the stellar continuum (grayscale) and Lyman-alpha (cyan contours). The centroids of each clump are marked with blue and red Xs , corresponding with stellar continuum and Ly α respectively. We explicitly label the different bright regions found within L1 and L2 in white lettering. The sigma levels of the Ly α contours are as follows: L1:[2,3,4], L2:[2,3], L3:[2,4,8,16], L4:[2,4,8], L5:[1,2], L6:[2,4,6].

4. ANALYSIS

4.1. Inferred Galaxy Properties

Due to the strong lensing magnification our lensed LAE galaxies have apparent brightnesses that are among the brightest LAEs discovered in blank field narrow-band surveys at similar redshifts, but are intrinsically much fainter than typical field LAEs (Figure 19) . In Table 5 we report the inferred stellar mass, age of the stellar population, and dust content (A_V). We compare our results with the

following studies: Chary et al. (2005); Gawiser et al. (2006); Lai et al. (2007); Pirzkal et al. (2007); Finkelstein et al. (2009); Hayes et al. (2013); Santos et al. (2021).

Our intrinsic stellar mass values are consistent with the other studies which find high-redshift LAEs having stellar masses $\sim 1 \times 10^7 M_\odot - 8.5 \times 10^9 M_\odot$. Our sample probes the low mass end of the $z \sim 4-5$ LAE mass functions (Santos et al. 2021). This is unsurprising given that gravitational lensing is a rare phenomenon and low mass LAEs are more numerous than high mass LAEs.

Our age measurements correspond with young stellar populations: $t_{50} \lesssim 30$ Myr. Young stellar populations create large amounts of Ly α , which is consistent with their high Ly α equivalent widths. The studies we compare against report ages $\sim 5 - 850$ Myr inferred through SED fitting. However, these values are obtained by fitting simple stellar population (SSP) or exponentially-decaying (tau-model) SFHs. Carnall et al. (2019) shows that use of these star-formation models imposes strong priors on physical parameters such as stellar population age. Our age measurements were inferred using non-parametric SFHs, which return galaxy properties with less bias and more accuracy (Leja et al. 2019). We find that the clumpy LAEs tend to be younger while the extended LAEs tend to be older, which we discuss further in Section 4.3.

We break dust attenuation into two categories: attenuation affecting young stellar populations (< 10 Myr, dust1) and attenuation affecting all older stellar populations (> 10 Myr, dust2). This distinction is based on the work of Charlot & Fall (2000). Physically, the attenuation in the birth clouds of young, massive stars can be different than the attenuation in regions where older stars have migrated away from their birth clouds. Older stellar populations may have had their surrounding gas disrupted through feedback from younger, more energetic stars. The studies to which we compare our data report dust extinctions from emission line diagnostics or SED fitting with only one dust component.

Our estimations for attenuation from young stellar populations (dust1) are consistent with these studies: having $A_V \sim 0 - 1$. We find that the LAEs with extended Ly α morphologies have larger A_V than those with clumpy Ly α . Since dust destroys Ly α photons, it is counter-intuitive to find more in

systems with extended Ly α . Our results imply that the main contributor to a clumpy vs. extended Ly α morphology is the H I distribution rather than the amount of dust.

4.2. *Ly α and UV Spatial Coincidence*

The measured image-plane spatial separation between the Ly α centroid and stellar continuum is reported in [Table 6](#) as $\delta_{Ly\alpha}$. Studies measuring large samples of field LAEs indicate that a significant portion contain a spatial offset. [Jiang et al. \(2013\)](#) found that there is little offset between UV and Ly α positions in compact galaxies ($< 0''.2$), but merging/interacting systems can be significantly offset ($> 0''.3$). [Shibuya et al. \(2014\)](#) found the majority of their LAE sample is offset by $< 0''.2$, yet only $\approx 23\%$ are classified as mergers. Our measurements do not take into account the distortion from gravitational lensing and should be considered upper limits to the true (source plane) separations. We find that all of the Ly α regions studied in our sample have small offsets $< 0''.2$, indicating that they are likely not merging nor interacting galaxies.

4.3. *LAE Morphology*

Robust quantitative descriptions of the Ly α morphology require forward modeling through the lensing potential. Efforts towards robust forward modeling of our LAE sample are currently underway. We present preliminary forward modeling results for L1 in the next section as evidence this method performs well. However, a more qualitative discussion of all our observed LAE morphologies deserves discussion.

In this section we present a qualitative discussion of the observed Ly α and stellar continuum morphologies for all our LAEs. One can see in [Figure 20](#) that the Ly α contours fall into two broad categories: extended and clumpy. L1, L2, and L5 have clumpy Ly α morphologies: the Ly α emission does not cover the entire galaxy, instead it is concentrated in specific regions. L3, L4, and L6 have extended morphologies: their Ly α emission covers the entire galaxy and extends beyond the associated stellar continuum emission. This broadening is consistent with Ly α radiative transfer.

We propose that our LAEs containing clumpy Ly α morphologies have varying H I column densities across their star-forming regions. Since H I scatters Ly α , lines of sight with lower H I column densities

preferentially allow more Ly α photons to escape. The Ly α clumps seen in our sample could be along these lines of sight. This hypothesis is supported by previous observations of Ly α emitting galaxies with evidence of non-uniform HI distributions (Heckman et al. 2011; Rivera-Thorsen et al. 2017; Chisholm et al. 2018; Gazagnes et al. 2018; Steidel et al. 2018). Furthermore, simulations of a similar galaxy in Blaizot et al. (2023) find significant anisotropic effects on the Ly α line shape and luminosity. These effects correlate with gas flows and evolve over short time scales (\sim tens Myr), implying the possibility of short-lived gas configurations that can create clumpy Ly α morphologies.

Our sample suggests a progression from clumpy Ly α to extended Ly α over a time scale of $\sim 14 - 38$ Myr based on t_{50} . The clumpy LAEs tend to be younger while the extended LAEs tend to be older. We note that L1 and L6 have similar ages while being classified differently, and explain this through our SFH resolution. Our first three SFH age bins cover (0,10] Myr, (10,30] Myr, and (30,61.7] Myr respectively. The upper error in t_{50} of L6 is larger than that of L1, extending beyond 30 Myr while L1 does not. This implies that the stellar population of L6 contains more older stars than that of L1. Due to the errors on the ages and our small sample size we do not claim that this observation is robust; instead merely suggestive.

A possible explanation of this apparent difference is that clumpy Ly α morphologies appear in a short-lived stage of starbursts. In this initial stage young massive stars ionize channels along preferential lines of sight. As more stars are formed and greater densities of ionizing photons are created, more lines of sight are punched through the ISM. These ionized channels allow Ly α to more easily directly escape the LAE through them into the IGM, explaining the presence of the clumpy Ly α morphologies. It is also possible that the inflowing gas that fuels bursts of star formation obscures lines of sight that would otherwise leak Ly α (Blaizot et al. 2023). However, not all Ly α that escapes a star forming region necessarily immediately exits into the IGM. Ionized channels allow Ly α to escape into the extended halo of neutral hydrogen that surrounds the LAE, where it can then scatter into an extended profile.

Band	Clump #	Half-Light Radius $r_{1/2}$	$r_{1/2}$	Amplitude I_e	Ellipticity e	Sérsic Index n
-	-	["]	[pc]	[erg/s/cm $^2 \times 10^{-3}$]	-	-
F125W	1	$0.00045^{+0.00050}_{-0.00014}$	$2.8^{+3.1}_{-0.9}$	$2.3^{+2.6}_{-1.8}$	$0.31^{+0.13}_{-0.18}$	$5.95^{+1.53}_{-1.92}$
Ly α	1	$0.00080^{+0.00039}_{-0.00027}$	$5.0^{+2.5}_{-1.7}$	$0.5^{+0.2}_{-0.2}$	$0.70^{+0.15}_{-0.32}$	$7.42^{+0.49}_{-2.04}$
F125W	2	$0.00003^{+0.00001}_{-0.00001}$	$0.2^{+<0.1}_{-<0.1}$	$791.9^{+576.0}_{-419.6}$	$0.46^{+0.20}_{-0.24}$	$3.73^{+2.25}_{-1.58}$
Ly α	2	$0.00004^{+0.00002}_{-0.00001}$	$0.3^{+0.1}_{-<0.1}$	$159.9^{+91.9}_{-110.4}$	$0.45^{+0.34}_{-0.31}$	$5.22^{+1.77}_{-2.15}$

Table 7: The recovered Sérsic parameters for each clump. We report the 16th, 50th and 84th percentiles of the posterior probability distributions. Note that the sizes of each clump in F125W and Ly α are statistically equivalent.

4.4. Preliminary Forward Modeling of L1

Here we present preliminary results for our forward modeling analysis of L1. L1 was chosen to be presented in this work because of the observation of multiple clumps in both the stellar continuum and Ly α and its brightness in Ly α . However, the image of L1 identified in Figure 12 is on the edge of the critical curve for this object’s redshift. Currently our code does not treat objects crossing the critical curve with rigor. Our models would likely cross this due to the distorted nature of the arc. Therefore, we chose to analyze the next brightest image of L1, which is farther removed from the critical curve. This image is located at 09:15:50.5 +38:24:54.4 and seen in Figure 21. The best fit Sérsic parameters are shown in Table 7 and corresponding models in Figure 21. The values and uncertainties of the Sérsic parameters are taken as the 16th, 50th, and 84th percentiles of their parameter distributions from the Emcee chain.

Comparing the half-light radius between F125W and Ly α in each clump, we see that they are statistically equivalent. This means that the size of the Ly α coming from each clump is similar to that of the stellar continuum. This supports the hypothesis that the clumpy morphology results from ionized channels allowing Ly α to escape along specific lines of sight. The anisotropic nature of these ionized channels would prevent the Ly α from appearing isotropic and extended across the

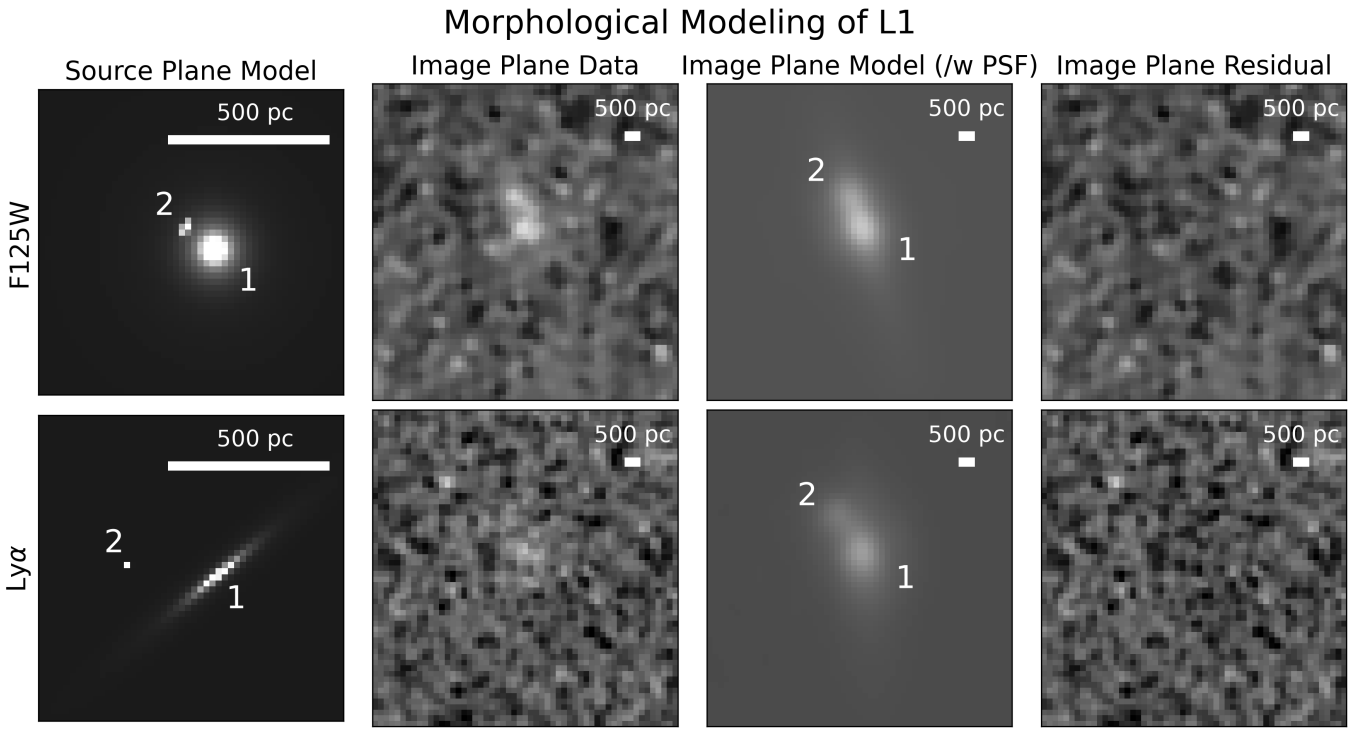


Figure 21: LAE Morphological modeling of an image of L1 located at 09:15:50.5 +38:24:54.4. We model two clumps in both the stellar continuum and Ly α . Models are created in the source plane (column one), passed through the lensing potential and convolved with a PSF (column three), and subtracted from the image-plane data (columns two and four). We model in the source plane on a 10x finer pixel grid compared to the image plane to account for native pixel distortion; this is represented by the scale bars. The clumps are labeled with their corresponding clump number in both the source-plane and image-plane models.

entire galaxy. The second clump is significantly smaller and brighter than the first. This could indicate a smaller ionized channel with a brighter star forming region in that part of the galaxy. The ellipticities and Sérsic indices are not well constrained: a consequence of PSF broadening and lensing model uncertainties. The convolution of the PSF with the models in the image plane makes multiple similar source-plane galaxy shapes appear equivalent in the image plane.

5. SUMMARY

We have investigated the image-plane properties of six Ly α emitting galaxies at $4.1 < z < 5.2$. Using multi-band imaging from HST and Spitzer, we were able to infer stellar mass, ages, and A_{Vs} with `Prospector`. Taking advantage of magnification from gravitational lensing and HST resolution narrowband filters we were able to measure Ly α on sub-galactic scales otherwise inaccessible. With the HST narrowband Ly α imaging we were able to see different types of Ly α morphology: clumpy vs. extended. Through use of lens models we were able to calculate the intrinsic stellar mass and Ly α luminosity. Finally, with our forward modeling code we were able to measure clump sizes of L1. Our findings are summarized below.

- The intrinsic stellar masses, ages, and amounts of dust are consistent with values from other studies of high and low redshift LAEs. In particular, the young ages of the stellar populations are consistent with the kinds of stars that produce high amounts of Ly α .
- The offsets between the stellar continuum and Ly α emission of our sample are small ($< 0.^{\prime\prime}2$). This is consistent with other studies which find small spatial offsets, and can be explained through radiative transfer through non-uniform HI distributions. The small offsets indicate our LAEs are not interacting nor merging systems.
- A qualitative analysis of the Ly α emission shows two broad categories of Ly α morphologies: clumpy and extended. We find that the LAEs containing clumpy Ly α generally have younger stellar populations. This suggests a possible progression from clumpy Ly α to extended Ly α , perhaps driven by the growth of young massive stars and creation of ionized channels during a starburst period.
- A forward modeling approach to modeling the morphology of L1 resulted in recovering Sérsic parameters for both bright clumps in both the stellar continuum and Ly α . We find that for each clump the sizes between F125W and the Ly α are statistically equivalent, suggesting the presence of ionized channels.

Future work Navarre et al. (in prep) will further study the source-plane (intrinsic) morphologies of this sample. That work will include the addition of rigorous treatments of models passing through the critical curve and calculation of source-plane (total) fluxes. We will also remeasure the Ly α offsets in the source plane and detail the new lens model for L6. We will directly compare the physical information with samples of low and high redshift LAEs, as well as with the inferred galaxy properties from this paper. We will characterize the variations in the morphology of the Ly α emission and compare them to low-redshift LAEs, where the distribution of Ly α is heterogeneous. (Bond et al. 2010; Finkelstein et al. 2011; Steidel et al. 2011; Feldmeier et al. 2013; Momose et al. 2014)

REFERENCES

- Alexandroff, R. M., Heckman, T. M., Borthakur, S., Overzier, R., & Leitherer, C. 2015, *The Astrophysical Journal*, 810, 104, doi: [10.1088/0004-637X/810/2/104](https://doi.org/10.1088/0004-637X/810/2/104)
- Atek, H., Labb  , I., Furtak, L. J., et al. 2023, arXiv e-prints, arXiv:2308.08540, doi: [10.48550/arXiv.2308.08540](https://doi.org/10.48550/arXiv.2308.08540)
- Bayliss, M. B., Hennawi, J. F., Gladders, M. D., et al. 2011, *The Astrophysical Journal Supplement Series*, 193, 8, doi: [10.1088/0067-0049/193/1/8](https://doi.org/10.1088/0067-0049/193/1/8)
- Bayliss, M. B., Rigby, J. R., Sharon, K., et al. 2014, *ApJ*, 790, 144, doi: [10.1088/0004-637X/790/2/144](https://doi.org/10.1088/0004-637X/790/2/144)
- Bayliss, M. B., Wuyts, E., Sharon, K., et al. 2010, *ApJ*, 720, 1559, doi: [10.1088/0004-637X/720/2/1559](https://doi.org/10.1088/0004-637X/720/2/1559)
- Berg, D. A., Erb, D. K., Auger, M. W., Pettini, M., & Brammer, G. B. 2018, *The Astrophysical Journal*, 859, 164, doi: [10.3847/1538-4357/aab7fa](https://doi.org/10.3847/1538-4357/aab7fa)
- Bertin, E., & Arnouts, S. 1996, *A&AS*, 117, 393, doi: [10.1051/aas:1996164](https://doi.org/10.1051/aas:1996164)
- Blaizot, J., Garel, T., Verhamme, A., et al. 2023, *MNRAS*, 523, 3749, doi: [10.1093/mnras/stad1523](https://doi.org/10.1093/mnras/stad1523)
- Bond, N. A., Feldmeier, J. J., Matkovi  , A., et al. 2010, *The Astrophysical Journal*, 716, L200, doi: [10.1088/2041-8205/716/2/l200](https://doi.org/10.1088/2041-8205/716/2/l200)
- Carnall, A. C., Leja, J., Johnson, B. D., et al. 2019, *The Astrophysical Journal*, 873, 44, doi: [10.3847/1538-4357/ab04a2](https://doi.org/10.3847/1538-4357/ab04a2)
- Charlot, S., & Fall, S. M. 2000, *ApJ*, 539, 718, doi: [10.1086/309250](https://doi.org/10.1086/309250)
- Chary, R.-R., Stern, D., & Eisenhardt, P. 2005, *ApJL*, 635, L5, doi: [10.1086/499205](https://doi.org/10.1086/499205)
- Chisholm, J., Gazagnes, S., Schaerer, D., et al. 2018, *A&A*, 616, A30, doi: [10.1051/0004-6361/201832758](https://doi.org/10.1051/0004-6361/201832758)
- Conroy, C., & Gunn, J. E. 2010, *ApJ*, 712, 833, doi: [10.1088/0004-637X/712/2/833](https://doi.org/10.1088/0004-637X/712/2/833)
- Conroy, C., Gunn, J. E., & White, M. 2009, *ApJ*, 699, 486, doi: [10.1088/0004-637X/699/1/486](https://doi.org/10.1088/0004-637X/699/1/486)
- Cowie, L. L., Barger, A. J., & Hu, E. M. 2011, *The Astrophysical Journal*, 738, 136, doi: [10.1088/0004-637x/738/2/136](https://doi.org/10.1088/0004-637x/738/2/136)
- Cowie, L. L., & Hu, E. M. 1998, *The Astronomical Journal*, 115, 1319, doi: [10.1086/300309](https://doi.org/10.1086/300309)
- Dawson, S., Rhoads, J. E., Malhotra, S., et al. 2007, *ApJ*, 671, 1227, doi: [10.1086/522908](https://doi.org/10.1086/522908)
- Deharveng, J.-M., Small, T., Barlow, T. A., et al. 2008, *The Astrophysical Journal*, 680, 1072, doi: [10.1086/587953](https://doi.org/10.1086/587953)
- Dijkstra, M. 2017, *Saas-Fee Lecture Notes: Physics of Lyman Alpha Radiative Transfer*, arXiv, doi: [10.48550/ARXIV.1704.03416](https://doi.org/10.48550/ARXIV.1704.03416)
- Dressler, A., Martin, C. L., Henry, A., Sawicki, M., & McCarthy, P. 2011, *The Astrophysical Journal*, 740, 71, doi: [10.1088/0004-637x/740/2/71](https://doi.org/10.1088/0004-637x/740/2/71)

- Erb, D. K., Berg, D. A., Auger, M. W., et al. 2019, ApJ, 884, 7, doi: [10.3847/1538-4357/ab3daf](https://doi.org/10.3847/1538-4357/ab3daf)
- Feldmeier, J. J., Hagen, A., Ciardullo, R., et al. 2013, The Astrophysical Journal, 776, 75, doi: [10.1088/0004-637X/776/2/75](https://doi.org/10.1088/0004-637X/776/2/75)
- Finkelstein, S. L., Malhotra, S., Rhoads, J. E., Hathi, N. P., & Pirzkal, N. 2009, Monthly Notices of the Royal Astronomical Society, 393, 1174, doi: [10.1111/j.1365-2966.2008.14256.x](https://doi.org/10.1111/j.1365-2966.2008.14256.x)
- Finkelstein, S. L., Rhoads, J. E., Malhotra, S., Grogin, N., & Wang, J. 2008, The Astrophysical Journal, 678, 655, doi: [10.1086/525272](https://doi.org/10.1086/525272)
- Finkelstein, S. L., Cohen, S. H., Windhorst, R. A., et al. 2011, The Astrophysical Journal, 735, 5, doi: [10.1088/0004-637X/735/1/5](https://doi.org/10.1088/0004-637X/735/1/5)
- Florian, M. K., Rigby, J. R., Acharyya, A., et al. 2021, ApJ, 916, 50, doi: [10.3847/1538-4357/ac0257](https://doi.org/10.3847/1538-4357/ac0257)
- Foreman-Mackey, D., Hogg, D. W., Lang, D., & Goodman, J. 2013, PASP, 125, 306, doi: [10.1086/670067](https://doi.org/10.1086/670067)
- Gawiser, E., van Dokkum, P. G., Gronwall, C., et al. 2006, ApJL, 642, L13, doi: [10.1086/504467](https://doi.org/10.1086/504467)
- Gazagnes, S., Chisholm, J., Schaeerer, D., et al. 2018, A&A, 616, A29, doi: [10.1051/0004-6361/201832759](https://doi.org/10.1051/0004-6361/201832759)
- Gladders, M. D., Hoekstra, H., Yee, H. K. C., Hall, P. B., & Barrientos, L. F. 2003, ApJ, 593, 48, doi: [10.1086/376518](https://doi.org/10.1086/376518)
- Gladders, M. D., Yee, H. K. C., & Ellingson, E. 2002, AJ, 123, 1, doi: [10.1086/324637](https://doi.org/10.1086/324637)
- Gonzaga, S., Hack, W., Fruchter, A., & Mack, J. 2012, The DrizzlePac Handbook
- Grazian, A., Boutsia, K., Giallongo, E., et al. 2023, arXiv e-prints, arXiv:2307.12421, doi: [10.48550/arXiv.2307.12421](https://doi.org/10.48550/arXiv.2307.12421)
- Gronke, M., Bull, P., & Dijkstra, M. 2015, ApJ, 812, 123, doi: [10.1088/0004-637X/812/2/123](https://doi.org/10.1088/0004-637X/812/2/123)
- Gronke, M., & Dijkstra, M. 2014, MNRAS, 444, 1095, doi: [10.1093/mnras/stu1513](https://doi.org/10.1093/mnras/stu1513)
- Gronke, M., Dijkstra, M., McCourt, M., & Oh, S. P. 2016, ApJL, 833, L26, doi: [10.3847/2041-8213/833/2/L26](https://doi.org/10.3847/2041-8213/833/2/L26)
- Gronke, M., Dijkstra, M., McCourt, M., & Oh, S. P. 2017, arXiv: Astrophysics of Galaxies. <https://api.semanticscholar.org/CorpusID:55304296>
- Gronwall, C., Ciardullo, R., Hickey, T., et al. 2007, The Astrophysical Journal, 667, 79, doi: [10.1086/520324](https://doi.org/10.1086/520324)
- Guaita, L., Acquaviva, V., Padilla, N., et al. 2011, The Astrophysical Journal, 733, 114, doi: [10.1088/0004-637X/733/2/114](https://doi.org/10.1088/0004-637X/733/2/114)
- Guaita, L., Melinder, J., Hayes, M., et al. 2015, A&A, 576, A51, doi: [10.1051/0004-6361/201425053](https://doi.org/10.1051/0004-6361/201425053)
- Hayes, M., Östlin, G., Schaeerer, D., et al. 2013, The Astrophysical Journal, 765, L27, doi: [10.1088/2041-8205/765/2/l27](https://doi.org/10.1088/2041-8205/765/2/l27)
- Heckman, T. M., Borthakur, S., Overzier, R., et al. 2011, The Astrophysical Journal, 730, 5, doi: [10.1088/0004-637X/730/1/5](https://doi.org/10.1088/0004-637X/730/1/5)

- Henry, A., Scarlata, C., Martin, C. L., & Erb, D. 2015, ApJ, 809, 19,
doi: [10.1088/0004-637X/809/1/19](https://doi.org/10.1088/0004-637X/809/1/19)
- Herrero Alonso, Y., Wisotzki, L., Miyaji, T., et al. 2023, A&A, 677, A125,
doi: [10.1051/0004-6361/202347294](https://doi.org/10.1051/0004-6361/202347294)
- Hu, W., Martin, C. L., Gronke, M., et al. 2023, arXiv e-prints, arXiv:2307.04911,
doi: [10.48550/arXiv.2307.04911](https://doi.org/10.48550/arXiv.2307.04911)
- Inoue, A. K., Shimizu, I., Iwata, I., & Tanaka, M. 2014, MNRAS, 442, 1805,
doi: [10.1093/mnras/stu936](https://doi.org/10.1093/mnras/stu936)
- Izotov, Y. I., Worseck, G., Schaerer, D., et al. 2021, MNRAS, 503, 1734,
doi: [10.1093/mnras/stab612](https://doi.org/10.1093/mnras/stab612)
- . 2018, MNRAS, 478, 4851,
doi: [10.1093/mnras/sty1378](https://doi.org/10.1093/mnras/sty1378)
- Jaskot, A. E., & Oey, M. S. 2014, ApJL, 791, L19,
doi: [10.1088/2041-8205/791/2/L19](https://doi.org/10.1088/2041-8205/791/2/L19)
- Jiang, L., Egami, E., Fan, X., et al. 2013, ApJ, 773, 153, doi: [10.1088/0004-637X/773/2/153](https://doi.org/10.1088/0004-637X/773/2/153)
- Johnson, B. D., Leja, J., Conroy, C., & Speagle, J. S. 2021, ApJS, 254, 22,
doi: [10.3847/1538-4365/abef67](https://doi.org/10.3847/1538-4365/abef67)
- Joye, W. A., & Mandel, E. 2003, in Astronomical Society of the Pacific Conference Series, Vol. 295, Astronomical Data Analysis Software and Systems XII, ed. H. E. Payne, R. I. Jedrzejewski, & R. N. Hook, 489
- Jullo, E., Kneib, J.-P., Limousin, M., et al. 2007, New Journal of Physics, 9, 447,
doi: [10.1088/1367-2630/9/12/447](https://doi.org/10.1088/1367-2630/9/12/447)
- Jung, I., Finkelstein, S. L., Arrabal Haro, P., et al. 2023, arXiv e-prints, arXiv:2304.05385,
doi: [10.48550/arXiv.2304.05385](https://doi.org/10.48550/arXiv.2304.05385)
- Kashikawa, N., Shimasaku, K., Matsuda, Y., et al. 2011, ApJ, 734, 119,
doi: [10.1088/0004-637X/734/2/119](https://doi.org/10.1088/0004-637X/734/2/119)
- Kikuta, S., Ouchi, M., Shibuya, T., et al. 2023, arXiv e-prints, arXiv:2305.08921,
doi: [10.48550/arXiv.2305.08921](https://doi.org/10.48550/arXiv.2305.08921)
- Kim, K. J., Malhotra, S., Rhoads, J. E., & Yang, H. 2021, ApJ, 914, 2,
doi: [10.3847/1538-4357/abf833](https://doi.org/10.3847/1538-4357/abf833)
- Kim, K. J., Bayliss, M. B., Rigby, J. R., et al. 2023, ApJL, 955, L17,
doi: [10.3847/2041-8213/acf0c5](https://doi.org/10.3847/2041-8213/acf0c5)
- Kramarenko, I. G., Kerutt, J., Verhamme, A., et al. 2023, arXiv e-prints, arXiv:2305.07044,
doi: [10.48550/arXiv.2305.07044](https://doi.org/10.48550/arXiv.2305.07044)
- Lai, K., Huang, J.-S., Fazio, G., et al. 2007, The Astrophysical Journal, 655, 704,
doi: [10.1086/510285](https://doi.org/10.1086/510285)
- Leja, J., Carnall, A. C., Johnson, B. D., Conroy, C., & Speagle, J. S. 2019, The Astrophysical Journal, 876, 3, doi: [10.3847/1538-4357/ab133c](https://doi.org/10.3847/1538-4357/ab133c)
- Limousin, M., Richard, J., Jullo, E., et al. 2007, The Astrophysical Journal, 668, 643,
doi: [10.1086/521293](https://doi.org/10.1086/521293)
- Madau, P. 1995, ApJ, 441, 18, doi: [10.1086/175332](https://doi.org/10.1086/175332)
- Madau, P., & Haardt, F. 2015, The Astrophysical Journal Letters, 813, L8,
doi: [10.1088/2041-8205/813/1/L8](https://doi.org/10.1088/2041-8205/813/1/L8)

- Marques-Chaves, R., Pérez-Fournon, I., Shu, Y., et al. 2017, ApJL, 834, L18,
doi: [10.3847/2041-8213/834/2/L18](https://doi.org/10.3847/2041-8213/834/2/L18)
- Masters, D., Capak, P., Salvato, M., et al. 2012, The Astrophysical Journal, 755, 169,
doi: [10.1088/0004-637X/755/2/169](https://doi.org/10.1088/0004-637X/755/2/169)
- Matsuoka, Y., Onoue, M., Iwasawa, K., et al. 2023, ApJL, 949, L42,
doi: [10.3847/2041-8213/acd69f](https://doi.org/10.3847/2041-8213/acd69f)
- Medina, J., Mack, J., & Calamida, A. 2022, WFC3/UVIS Encircled Energy, Instrument Science Report WFC3 2022-2, 23 pages
- Michel-Dansac, L., Blaizot, J., Garel, T., et al. 2020, Astronomy & Astrophysics, 635,
doi: [10.1051/0004-6361/201834961](https://doi.org/10.1051/0004-6361/201834961)
- Momose, R., Ouchi, M., Nakajima, K., et al. 2014, Monthly Notices of the Royal Astronomical Society, 442, 110, doi: [10.1093/mnras/stu825](https://doi.org/10.1093/mnras/stu825)
- Mukae, S., Ouchi, M., Hill, G. J., et al. 2020, ApJ, 903, 24, doi: [10.3847/1538-4357/abb81b](https://doi.org/10.3847/1538-4357/abb81b)
- Navarre, A. 2023a, Replication HST Narrowband Data for: Resolving Clumpy vs. Extended Ly- α In Strongly Lensed, High-Redshift Ly- α Emitters, Harvard Dataverse,
doi: [10.7910/DVN/9Q0YYW](https://doi.org/10.7910/DVN/9Q0YYW)
- . 2023b, Replication Spitzer Data for: Resolving Clumpy vs. Extended Ly- α In Strongly Lensed, High-Redshift Ly- α Emitters, Harvard Dataverse, doi: [10.7910/DVN/JSVGGM8](https://doi.org/10.7910/DVN/JSVGGM8)
- Ono, Y., Shimasaku, K., Dunlop, J., et al. 2010, The Astrophysical Journal, 724, 1524,
doi: [10.1088/0004-637x/724/2/1524](https://doi.org/10.1088/0004-637x/724/2/1524)
- Östlin, G., Hayes, M., Kunth, D., et al. 2009, AJ, 138, 923, doi: [10.1088/0004-6256/138/3/923](https://doi.org/10.1088/0004-6256/138/3/923)
- Ouchi, M., Shimasaku, K., Akiyama, M., et al. 2008, ApJS, 176, 301, doi: [10.1086/527673](https://doi.org/10.1086/527673)
- Palanque-Delabrouille, N., Magneville, Ch., Yèche, Ch., et al. 2013, A&A, 551, A29,
doi: [10.1051/0004-6361/201220379](https://doi.org/10.1051/0004-6361/201220379)
- Peng, C. Y., Ho, L. C., Impey, C. D., & Rix, H.-W. 2010, AJ, 139, 2097,
doi: [10.1088/0004-6256/139/6/2097](https://doi.org/10.1088/0004-6256/139/6/2097)
- Pirzkal, N., Malhotra, S., Rhoads, J. E., & Xu, C. 2007, The Astrophysical Journal, 667, 49,
doi: [10.1086/519485](https://doi.org/10.1086/519485)
- Rasekh, A., Melinder, J., Östlin, G., et al. 2022, A&A, 662, A64,
doi: [10.1051/0004-6361/202140734](https://doi.org/10.1051/0004-6361/202140734)
- Rhoads, J. E., Malhotra, S., Dey, A., et al. 2000, The Astrophysical Journal, 545, L85,
doi: [10.1086/317874](https://doi.org/10.1086/317874)
- Ricci, F., Marchesi, S., Shankar, F., La Franca, F., & Civano, F. 2016, Monthly Notices of the Royal Astronomical Society, 465, 1915,
doi: [10.1093/mnras/stw2909](https://doi.org/10.1093/mnras/stw2909)
- Rivera-Thorsen, T. E., Dahle, H., Gronke, M., et al. 2017, A&A, 608, L4,
doi: [10.1051/0004-6361/201732173](https://doi.org/10.1051/0004-6361/201732173)
- Robertson, B. E. 2022, Annual Review of Astronomy and Astrophysics, 60, 121,
doi: [10.1146/annurev-astro-120221-044656](https://doi.org/10.1146/annurev-astro-120221-044656)
- Roy, N., Henry, A., Treu, T., et al. 2023, ApJL, 952, L14, doi: [10.3847/2041-8213/acdbce](https://doi.org/10.3847/2041-8213/acdbce)

- Runnholm, A., Hayes, M. J., Lin, Y.-H., et al. 2023, MNRAS, 522, 4275, doi: [10.1093/mnras/stad1264](https://doi.org/10.1093/mnras/stad1264)
- Rzepecki, J., Lombardi, M., Rosati, P., Bignamini, A., & Tozzi, P. 2007, A&A, 471, 743, doi: [10.1051/0004-6361:20077594](https://doi.org/10.1051/0004-6361:20077594)
- Saldana-Lopez, A., Schaefer, D., Chisholm, J., et al. 2023, MNRAS, 522, 6295, doi: [10.1093/mnras/stad1283](https://doi.org/10.1093/mnras/stad1283)
- Salim, S., & Narayanan, D. 2020, ARA&A, 58, 529, doi: [10.1146/annurev-astro-032620-021933](https://doi.org/10.1146/annurev-astro-032620-021933)
- Santos, S., Sobral, D., Butterworth, J., et al. 2021, MNRAS, 505, 1117, doi: [10.1093/mnras/stab1218](https://doi.org/10.1093/mnras/stab1218)
- Scarlata, C., Colbert, J., Teplitz, H. I., et al. 2009, ApJL, 704, L98, doi: [10.1088/0004-637X/704/2/L98](https://doi.org/10.1088/0004-637X/704/2/L98)
- Semelin, B., Combes, F., & Baek, S. 2007, Astronomy and Astrophysics, 474, 365. <https://api.semanticscholar.org/CorpusID:264605192>
- Sharon, K., Bayliss, M. B., Dahle, H., et al. 2020, ApJS, 247, 12, doi: [10.3847/1538-4365/ab5f13](https://doi.org/10.3847/1538-4365/ab5f13)
- Sharon, Keren. 2022, SDSS Giant Arcs Survey ("SGAS"), STScI/MAST, doi: [10.17909/T9-CQTJ-Y020](https://doi.org/10.17909/T9-CQTJ-Y020)
- Shibuya, T., Ouchi, M., Nakajima, K., et al. 2014, ApJ, 785, 64, doi: [10.1088/0004-637X/785/1/64](https://doi.org/10.1088/0004-637X/785/1/64)
- Smit, R., Swinbank, A. M., Massey, R., et al. 2017, MNRAS, 467, 3306, doi: [10.1093/mnras/stx245](https://doi.org/10.1093/mnras/stx245)
- Steidel, C. C., Bogosavljević, M., Shapley, A. E., et al. 2011, The Astrophysical Journal, 736, 160, doi: [10.1088/0004-637x/736/2/160](https://doi.org/10.1088/0004-637x/736/2/160)
- Steidel, C. C., Bogosavljević, M., Shapley, A. E., et al. 2018, The Astrophysical Journal, 869, 123, doi: [10.3847/1538-4357/aaed28](https://doi.org/10.3847/1538-4357/aaed28)
- Swinbank, A. M., Bower, R. G., Smith, G. P., et al. 2007, MNRAS, 376, 479, doi: [10.1111/j.1365-2966.2007.11454.x](https://doi.org/10.1111/j.1365-2966.2007.11454.x)
- Thai, T. T., Tuan-Anh, P., Pello, R., et al. 2023, arXiv e-prints, arXiv:2308.08685, doi: [10.48550/arXiv.2308.08685](https://doi.org/10.48550/arXiv.2308.08685)
- Verhamme, A., Orlitová, I., Schaefer, D., et al. 2017, A&A, 597, A13, doi: [10.1051/0004-6361/201629264](https://doi.org/10.1051/0004-6361/201629264)
- Verhamme, A., Garel, T., Ventou, E., et al. 2018, MNRAS, 478, L60, doi: [10.1093/mnrasl/sly058](https://doi.org/10.1093/mnrasl/sly058)
- Verhamme, Anne, Orlitová, Ivana, Schaefer, Daniel, & Hayes, Matthew. 2015, A&A, 578, A7, doi: [10.1051/0004-6361/201423978](https://doi.org/10.1051/0004-6361/201423978)
- Wambsganss, J. 1998, Living Reviews in Relativity, 1, 12, doi: [10.12942/lrr-1998-12](https://doi.org/10.12942/lrr-1998-12)
- Welch, B., Coe, D., Diego, J. M., et al. 2022, Nature, 603, 815, doi: [10.1038/s41586-022-04449-y](https://doi.org/10.1038/s41586-022-04449-y)
- Witstok, J., Smit, R., Maiolino, R., et al. 2021, MNRAS, 508, 1686, doi: [10.1093/mnras/stab2591](https://doi.org/10.1093/mnras/stab2591)
- Witstok, J., Smit, R., Saxena, A., et al. 2023, arXiv e-prints, arXiv:2306.04627, doi: [10.48550/arXiv.2306.04627](https://doi.org/10.48550/arXiv.2306.04627)

Yamada, S. F., Sasaki, S. S., Sumiya, R., et al.
2005, Publications of the Astronomical Society
of Japan, 57, 881, doi: [10.1093/pasj/57.6.881](https://doi.org/10.1093/pasj/57.6.881)
Yang, H., Malhotra, S., Rhoads, J. E., et al. 2017,
ApJ, 838, 4, doi: [10.3847/1538-4357/aa6337](https://doi.org/10.3847/1538-4357/aa6337)
York, D. G., Adelman, J., Anderson, John E., J.,
et al. 2000, AJ, 120, 1579, doi: [10.1086/301513](https://doi.org/10.1086/301513)

Zackrisson, E., Inoue, A. K., & Jensen, H. 2013,
ApJ, 777, 39, doi: [10.1088/0004-637X/777/1/39](https://doi.org/10.1088/0004-637X/777/1/39)
Östlin, G., Hayes, M., Duval, F., et al. 2014, The
Astrophysical Journal, 797, 11,
doi: [10.1088/0004-637x/797/1/11](https://doi.org/10.1088/0004-637x/797/1/11)